No.: egusphere-2023-2913

Title: Measurement Report: Elevated excess-NH_3 can promote the redox reaction to produce HONO: Insights from the COVID-19 pandemic

Reviewer #2:

General Comments:

This study reported that there was a noticeable increase in NH_3 concentrations during the COVID-19 pandemic. In addition to the meteorological conditions, the significant decrease in sulfate and nitrate concentrations enhanced the portioning of NH_4^+ to NH_3, which enables enhanced particle pH values and in turn accelerate the redox reactions between NO_2 and SO_2 to form HONO. The article has several major issues and should be considered carefully.

Thank you for your careful reading of our paper and valuable comments and suggestions. We believe that we have adequately addressed your comments. To facilitate your review, we used green highlights for your comments, yellow highlights for Reviewer #1, and red color indicating our own corrections in the manuscript.

1. In the introduction, the author comments that the exact relationship between NO_x, NH_3 and AOC remains unclear. However, it's a lengthy description of the changes in NH_3 and pH before and during the epidemic and there is no detailed discussion on the specific impact on AOC. In short, the research problems pointed out in the introduction have not been fully explored in the study, and many conclusions are very far-fetched.

Response: Thanks for your comment. In the original article, we indeed overly extended the perspectives of this study. In the revised manuscript, we removed all descriptions regarding AOC and focused on the sources of HONO, for example:

"Nitrous acid (HONO) is a critical precursor of hydroxyl radical (OH), contributing to more than 60% of OH production (Alicke, 2003; Platt et al., 1980; Kleffmann et al., 2005). The OH can react with carbon monoxide, nitrogen oxides (NO_x), sulfur dioxide (SO_2), and volatile organic compounds to produce secondary pollutants such as ozone (O_3) and $PM_{2.5}$ (particulate matter with an aerodynamic diameter less than or equal to 2.5 μm), thereby affecting air quality, human health, and global climate change (Li et al., 2021a; Wang et al., 2023b; Lu et al., 2018)."

2. In lines 296-297, the paper argues that HONO has other sources and that the process of NO_2 reacting with SO_2 to generate HONO is currently insufficient evidence. In addition, this reaction is affected by pH, so how much does this contribution to HONO affect atmospheric oxidation? This discussion is also sorely lacking.

Response: Thanks for your comment. In recent years, an increasing number of laboratory and field observation studies have shown that the reaction of NO_2 and SO_2 can generate HONO, especially under high ammonia conditions (Ge et al., 20219; Li et al., 2018; Zhang et al., 2023, 2024). Accordingly, this study found that observed NH_3 concentrations increased during the epidemic control period, and calculated pH values showed an increase. In addition, the positive correlations between HONO with SO_2, Excess-NH_x, SO_4^{2-}, and pH further indicate the existence of reaction of NO_2 and SO_2.

Moreover, we calculated the reaction rate of NO_2 and SO_2 and found that it rose by more than 50%. Although the majority of HONO unknown sources remain unexplained, this partly explains the significant decrease in NO_x during the epidemic period, but the relatively low decrease in HONO concentrations.

Ge, S., Wang, G., Zhang, S., Li, D., and Zhang, H.: Abundant NH_3 in China enhances atmospheric HONO production by promoting the heterogeneous reaction of SO_2 with NO_2. Environ. Sci. Technol. 53, 14339 – 14347, https://doi.org/10.1021/acs.est.9b04196, 2019.

Li, L., Hoffmann, M. R., and Colussi, A. J.: Role of nitrogen dioxide in the production of sulfate during Chinese haze-aerosol episodes, Environ. Sci. Technol., 52, 2686 – 2693, https://doi.org/10.1021/acs.est.7b05222, 2018.

Zhang, X., Tong, S., Jia, C., Zhang, W., Wang, Z., Tang, G., Hu, B., Liu, Z., Wang, L., Zhao, P., Pan, Y., and Ge, M.: Elucidating HONO formation mechanism and its essential contribution to OH during haze events., npj. ClWim. Atmos. Sci., 6, 55, https://doi.org/10.1038/s41612-023-00371-w, 2023.

Zhang, P., Li, H., Ma, Q., Chen, T., Chu, B., Yu, Y., and He, H.: SO_2 photoaging enhances the surface conversion of NO_2-to-HONO on elemental carbon, Environ. Sci. Technol. Lett., 11, 143 – 149, https://doi.org/10.1021/acs.estlett.3c00878, 2024.

3. About HONO sources calculation, there are also many issues. The emission of motor vehicles at different stations varies greatly, so it is unreasonable to use 0.65% as the emission factor of HONO at all stations.

Response: Thanks for your comments.

Firstly, We determined whether it is necessary to calculate vehicle emissions, and a supplementary HONO emission factor table from vehicle emissions was added to support the selection of factors in the revised version:

"HONO can be released directly into the atmosphere through vehicle exhaust (Burling et al., 2010; Veres et al., 2010). The lifetime of HONO in the atmosphere is relatively short, so vehicle emissions significantly contribute to urban atmospheric HONO (Chen et al., 2023; Liu et al., 2021a). Considering that there has been a significant reduction in vehicle emissions in urban areas during DC. Additionally, the R-PY site is far from roads. Thus, vehicle emissions may not be the primary source of HONO for the U-ZK site during DC and R-PY sites during entire periods. To further validate the above conclusions, the conditional bivariate probability function diagrams of NO_2 at U-ZK and R-PY sites during PC and DC are depicted in Figure S2. NO_2 predominantly originated from long-distance transport at the U-ZK site during DC and the R-PY site during both PC and DC. Consequently, vehicle emissions are only calculated for the U-ZK site during the PC.

Here we use the HONO/NO_x ratio to estimate HONO concentration, which is generally considered to be the vehicle emission factor (Kramer et al., 2020; Hao et al., 2020; Yu et al., 2022) for HONO. The calculation formula is as follows:

$$[HONO_{emi}] = 0.8\% \times [NO_x] \quad (1)$$

where [$HONO_{emi}$] and [NO_x] represent the HONO concentration emitted by vehicles and the observed NO_x concentration, respectively. Regarding previous studies (Table S3), 0.8% was selected as the vehicle emission factor, considering differences in vehicle type, fuel composition, and other factors (Kramer et al., 2020; Hao et al., 2020; Huang et al., 2017)."

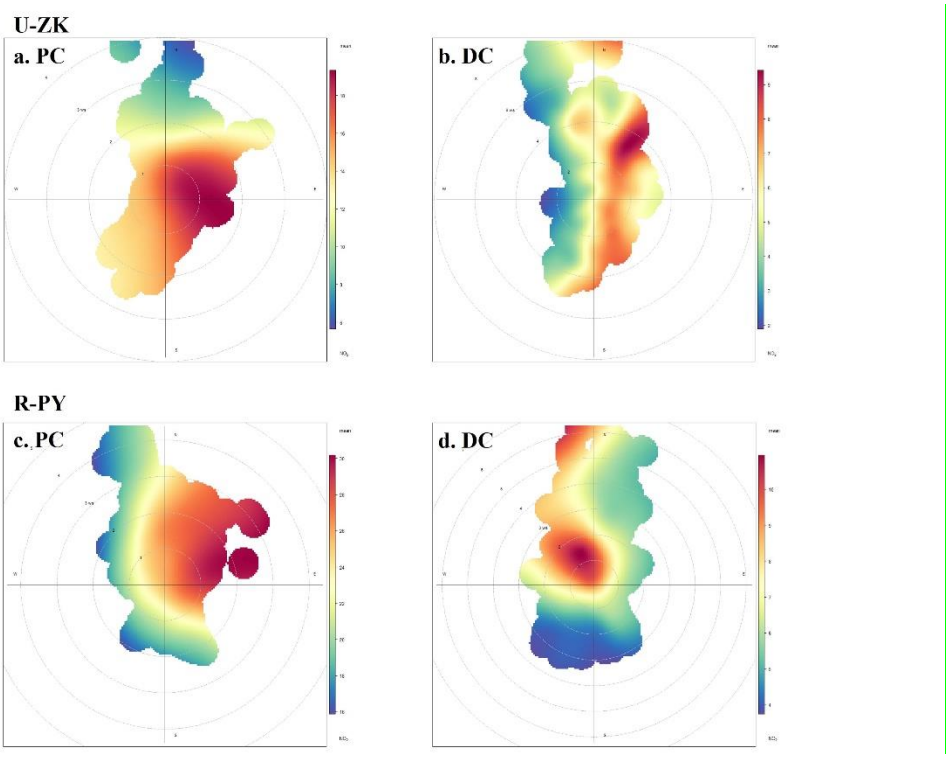

Figure S2. Result of conditional bivariate probability function plots: NO_2 at U-ZK and R-PY sites before (PC) and during (DC) the COVID-19 outbreak. The color scale bar represents NO_2 concentration.

Table S3. Summary of vehicle emission factors.

Observation site	Period	Emission factor (%)	Reference
Beijing	2020	0.79	(Meng et al., 2020)
Hong Kong	2015	0.4–1.8	(Yun et al., 2017)
Hong Kong	2011	0.5–1.6	(Xu et al., 2015)
Kiesberg Tunnel	2001	0.8	(Kleffmann et al., 2003)
Kiesberg Tunnel	1997	0.3–0.8	(Kurtenbach and Wiesen, 2001)
Guangzhou	2019	1.31	(Li et al., 2021b)

Secondly, the sources of HONO were recalculated to better investigate the changes in HONO between PC and DC periods:

Text S4 Sources of HONO

4.1 Direct emission

HONO can be released directly into the atmosphere through vehicle exhaust (Burling et al., 2010; Veres et al., 2010). The lifetime of HONO in the atmosphere is relatively short, so vehicle emissions significantly contribute to urban atmospheric HONO (Chen et al., 2023; Liu et al., 2021a). Considering that there has been a significant reduction in vehicle emissions in urban areas during DC. Additionally, the R-PY site is far from roads. Thus, vehicle emissions may not be the primary source of HONO for the U-ZK site during DC and R-PY sites during entire periods. To further validate the above conclusions, the conditional bivariate probability function diagrams of NO_2 at U-ZK and R-PY sites during PC and DC are depicted in Figure S2. NO_2 predominantly originated from long-distance transport at the U-ZK site during DC and the R-PY site during both PC and DC. Consequently, vehicle emissions are only calculated for the U-ZK site during the PC.

Here we use the HONO/NO_x ratio to estimate HONO concentration, which is generally considered to be the vehicle emission factor (Kramer et al., 2020; Hao et al., 2020; Yu et al., 2022) for HONO. The calculation formula is as follows：

$$[HONO_{emi}] = 0.8\% \times [NO_x] \quad (1)$$

where [$HONO_{emi}$] and [NO_x] represent the HONO concentration emitted by vehicles and the observed NO_x concentration, respectively. Regarding previous studies (Table S3), 0.8% was selected as the vehicle emission factor, considering differences in vehicle

type, fuel composition, and other factors (Kramer et al., 2020; Hao et al., 2020; Huang et al., 2017).

4.2 Homogeneous reaction of NO and •OH

The reaction between NO and •OH is the primary gas-phase reaction source of HONO at high NO concentrations, and the production rate contribution (P_{OH+NO}) for this reaction can be calculated as:

$$P_{OH+NO} = k_{OH+NO}[OH][NO] \quad (2)$$

where k_{OH+NO} (7.2×10^{-12} cm^3 $molecule^{-1}$ s^{-1}) is the rate constant for the reactions at 298K (Li et al., 2012). •OH concentration was simulated according to the empirical model (Hu et al., 2022; Wang et al., 2025):

$$[OH] = 4.1\times10^{9} \times \frac{J(O^1D)\times J(NO_2)\times(140\times[NO_2]+1)+[HONO]\times J(HONO)}{0.41\times[NO_2]^2+1.7\times[NO_2]+1+[NO]\times k_{NO+OH}+[HONO]\times k_{NO+OH}} \quad (3)$$

where, J (O^1 D), J (NO_2), and J (HONO) are the photolysis rates calculated using the TUV model (v5.2; available at http://cprm.acom.ucar.edu/Models/TUV/). The cloud optical depth value for the TUV model was adjusted so that the predicted UVB radiation intensity matched the observations (Lyu et al., 2019; Wang et al., 2022b). The calculated •OH concentration varied from 0.1×10^6 to 4×10^6 molecule/cm^3 at U-ZK and 0.1×10^6 to 5×10^6 molecule/cm^3 t R-PY, which was comparable to the levels in other cities of North China (Li et al., 2018; Fuchs et al., 2017; Yang et al., 2017). Since there is no photolysis at night, the •OH concentration was assumed to be 0.8×10^6 molecule/cm^3 (Wang et al., 2022).

4.3 Heterogeneous conversion of NO_2 to HONO

4.3.1 Heterogeneous dark reactions

The heterogeneous conversion of NO_2 to HONO on the ground (P_{ground}) and on the aerosol surface ($P_{aerosol}$) was calculated based on parameters obtained from experiments or observations.

$$P_{ground} = \frac{1}{8}\gamma_1 \times [NO_2] \times C_{NO_2} \times \frac{S_g}{V} \quad (4)$$

$$P_{aerosol} = \frac{1}{4}\gamma_2 \times [NO_2] \times C_{NO_2} \times \frac{S_a}{V} \quad (5)$$

$$\frac{S_g}{V} = \frac{1}{MLH} \quad (6)$$

$$C_{NO_2} = \sqrt{\frac{8RT}{\pi M}} \quad (7)$$

where C_{NO2} is the average molecular velocity of NO_2 molecule (m s^{-1}); R is the ideal gas constant; T is the temperature (K); M is the molecular weight of NO_2 (kg mol^{-1}); MLH is the height of the mixed layer, which is determined to be 50 m due to HONO formation on the ground level and its short lifetime (Liu et al., 2020b); S_a/V is the surface area to volume ratio of aerosol, estimated by Su et al. (Su et al., 2008).

4.3.2 Heterogeneous photo-enhanced reactions

The heterogeneous photo-enhanced reactions of NO_2 on the surface of the ground ($P_{ground + hv}$) and the surface of the aerosol ($P_{aerosol + hv}$) were calculated following (Zhang et al., 2020a):

$$P_{ground+hv} = \frac{1}{8} \times C_{NO_2} \times \frac{1}{MLH} \times \gamma_1 \times \frac{J_{NO_2}}{J_{NO_2,noon}} \times [NO_2] \quad (8)$$

$$P_{aerosol+hv} = \frac{1}{4} \times C_{NO_2} \times \frac{S_a}{V} \times \gamma_2 \times \frac{J_{NO_2}}{J_{NO_2,noon}} \times [NO_2] \quad (9)$$

where JNO_2 and $JNO_{2,noon}$ are the photolysis rate of NO_2 and the photolysis rate of NO_2 at noon during the day, respectively.

γ_1 and γ_2 are the absorption coefficient of NO_2 on the ground and aerosol surface, respectively, which is assumed to be 4×10^{-6} (Yu et al., 2022; Zhang et al., 2021; Zhang et al., 2020a). Moreover, we discuss the uncertainties based on the recommended values of 2×10^{-6}–1×10^{-5} as upper and lower bounds(Chen et al., 2023; VandenBoer et al., 2013; Wong et al., 2011). Results show (Figure S3) that the uncertainties for P_{ground}, $P_{aerosol}$, $P_{groung+hv}$, and $P_{aerosol+hv}$ are −50% to 150%, −50% to 151%, −20% to 120%, and −50% to 121% at the U-ZK, respectively. At the R-PY, the uncertainties for P_{ground}, $P_{aerosol}$, $P_{groung+hv}$, and $P_{aerosol+hv}$ are −50% to 150%, −50% to 151%, −20% to 120%, and −50% to 121%, respectively.

4.4 Nitrate photolysis

The nitrate photolysis ($P_{nitrate}$) was calculated based on the measured nitrate concentration (NO_3^-) from $PM_{2.5}$ and nitrate photolysis rate ($J_{nitrate \rightarrow HONO}$):

$$P_{nitrate} = J_{nitrate \rightarrow HONO} \times [NO_3^-] \quad (10)$$

where the $J_{nitrate \rightarrow HONO}$ was simulated by normalizing UV values, when the Zenit Angle is 0°, $J_{nitrate \rightarrow HONO}$ varied within the range of 1.22×10^{-5} to 4.84×10^{-4} s^{-1}, with an average value of 8.24×10^{-5} s^{-1} (Bao et al., 2018).”

Unfortunately, for MLH, S_a/V, and the relationship between k1 and temperature, as there were no observational data or scientifically established estimation methods, this study did not consider their variations. This omission may lead to differences in conclusions and warrants further investigation in future research.

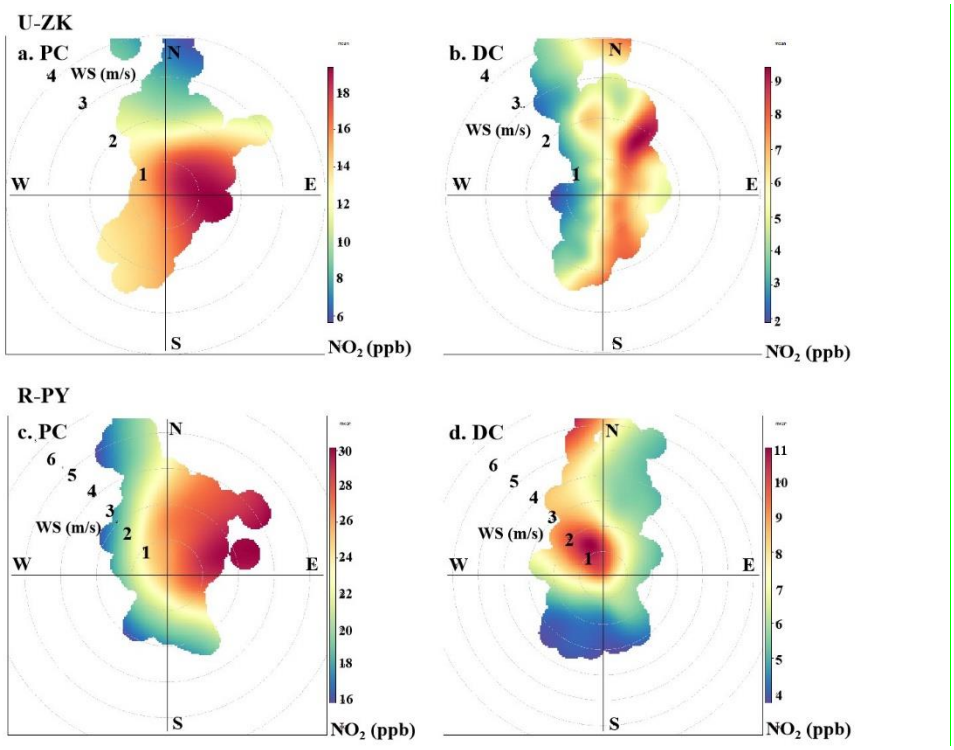

Figure S2. Result of conditional bivariate probability function plots: NO_2 at U-ZK and R-PY sites before (PC) and during (DC) the COVID-19 outbreak. The color scale bar represents NO_2 concentration.

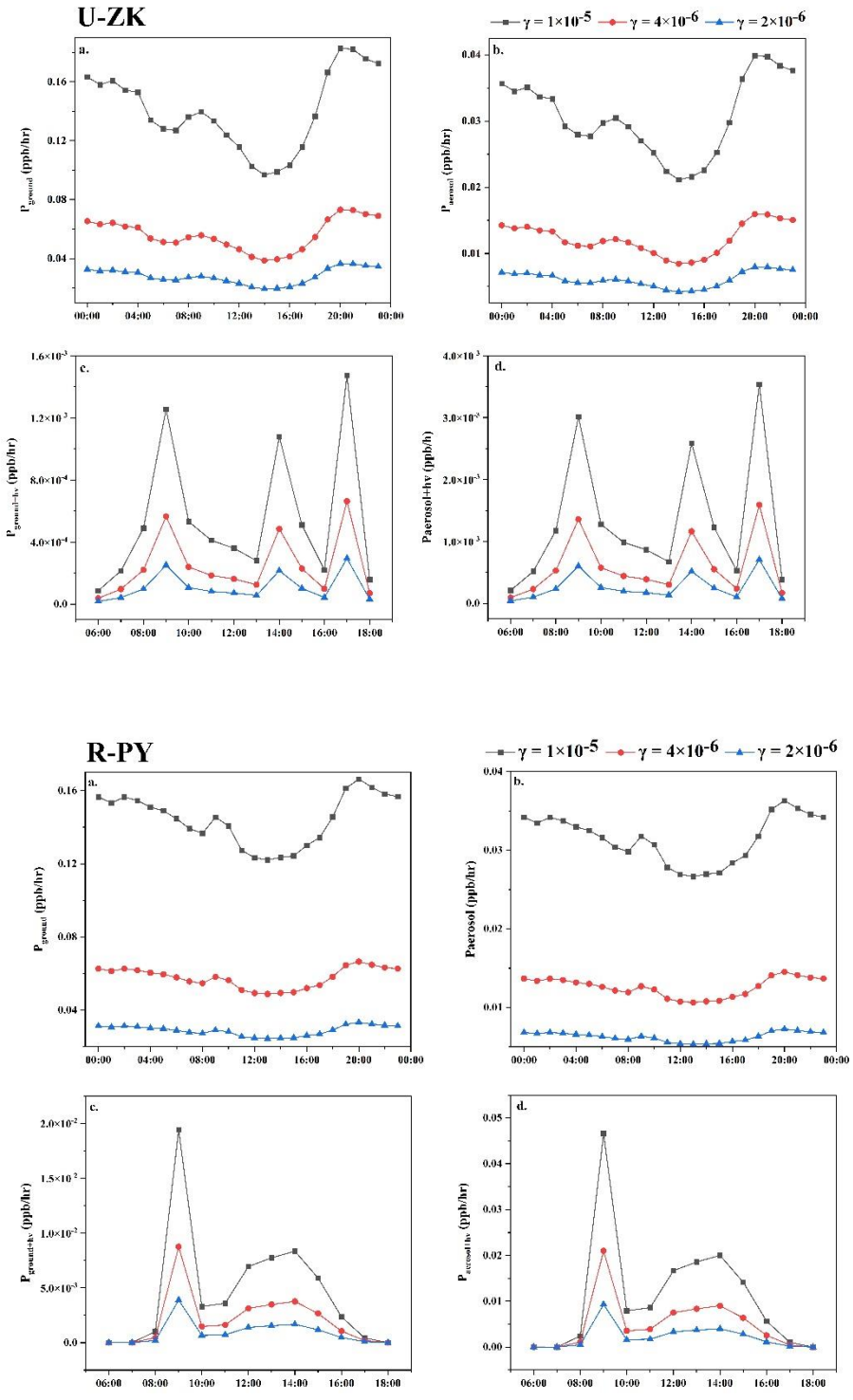

Figure S3. HONO production rate using different uptake rates of NO_2 at the U-ZK and R-PY sites before (PC) and during (DC) the COVID-19 outbreak. (a)P_{ground}, (b) $P_{aerosol}$, (c) $P_{ground+hv}$, and (d) $P_{aerosol+hv}$

Table S3. Summary of vehicle emission factors.

Observation site	Period	Emission factor (%)	Reference
Beijing	2020	0.79	(Meng et al., 2020)
Hong Kong	2015	0.4–1.8	(Yun et al., 2017)
Hong Kong	2011	0.5–1.6	(Xu et al., 2015)
Kiesberg Tunnel	2001	0.8	(Kleffmann et al., 2003)
Kiesberg Tunnel	1997	0.3–0.8	(Kurtenbach and Wiesen, 2001)
Guangzhou	2019	1.31	(Li et al., 2021b)

4. The uptake coefficient of NO_2 on surfaces is not mentioned.

Response: Thank you for your comment. We have added the description of the uptake coefficient of NO_2:

"γ_1 and γ_2 are the absorption coefficient of NO_2 on the ground and aerosol surface, respectively, which is assumed to be 4×10^{-6} (Yu et al., 2022; Zhang et al., 2021; Zhang et al., 2020a). Moreover, we discuss the uncertainties based on the recommended values of 2×10^{-6}–1×10^{-5} as upper and lower bounds(Chen et al., 2023; VandenBoer et al., 2013; Wong et al., 2011). Results show (Figure S3) that the uncertainties for P_{ground}, $P_{aerosol}$, $P_{groung+hv}$, and $P_{aerosol+hv}$ are −50% to 150%, −50% to 151%, −20% to 120%, and −50% to 121% at the U-ZK, respectively. At the R-PY, the uncertainties for P_{ground}, $P_{aerosol}$, $P_{groung+hv}$, and $P_{aerosol+hv}$ are −50% to 150%, −50% to 151%, −20% to 120%, and −50% to 121%, respectively."

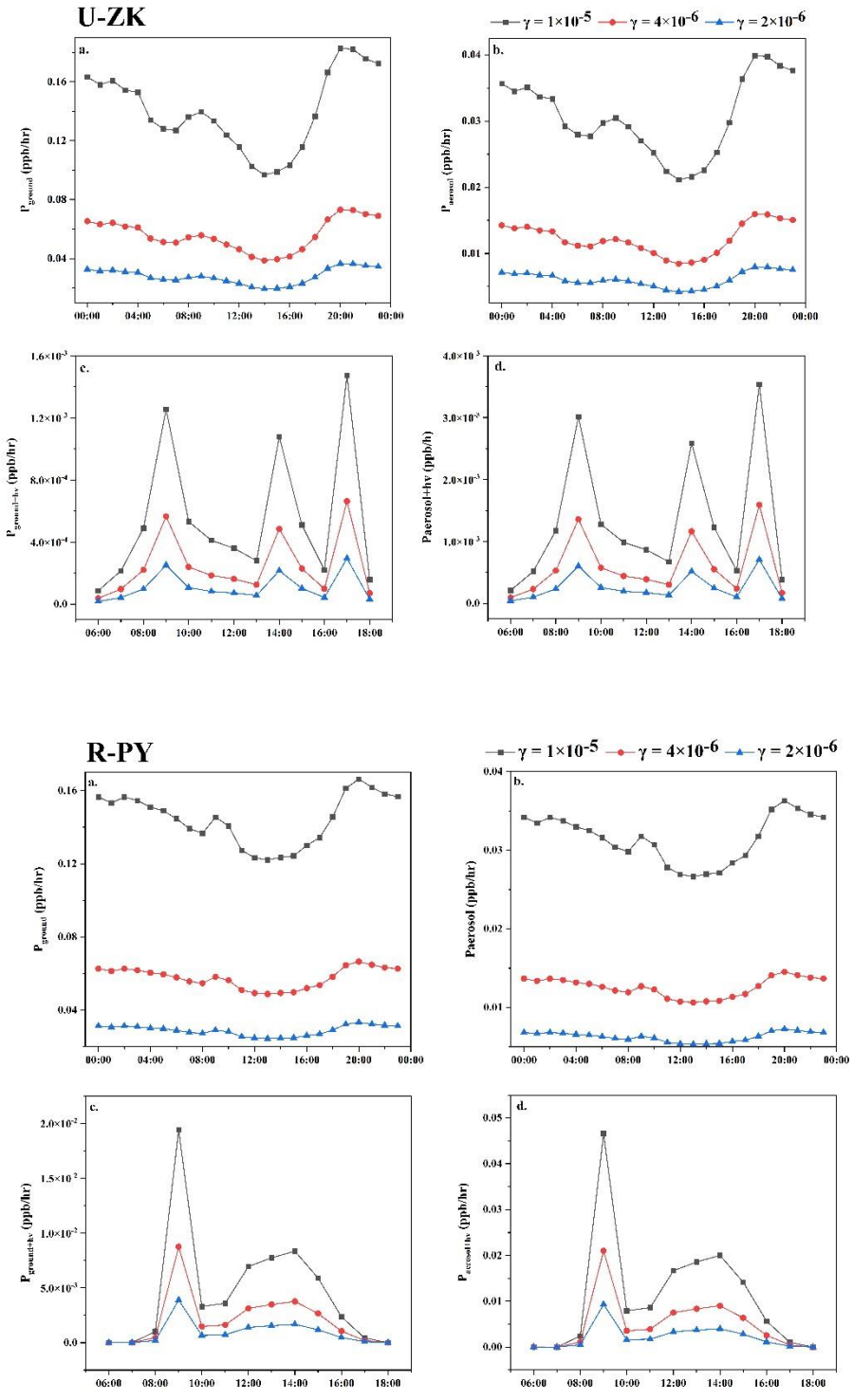

Figure S3. HONO production rate using different uptake rates of NO_2 at the U-ZK and R-PY sites before (PC) and during (DC) the COVID-19 outbreak. (a)P_{ground}, (b) $P_{aerosol}$, (c) $P_{ground+hv}$, and (d) $P_{aerosol+hv}$

5. The same OH concentration used at all station is also controversial.

Response: Thank you for your comments. We have modified the method for determining •OH concentration in the revised manuscript:

•OH concentration was simulated according to the empirical model (Hu et al., 2022; Wang et al., 2025):

$$[OH] = 4.1\times10^{9}\times\frac{J(O^{1}D)\times J(NO_2)\times(140\times[NO_2]+1)+[HONO]\times J(HONO)}{0.41\times[NO_2]^{2}+1.7\times[NO_2]+1+[NO]\times k_{NO+OH}+[HONO]\times k_{NO+OH}} \quad (3)$$

where, J (O^1 D), J (NO_2), and J (HONO) are the photolysis rates calculated using the TUV model (v5.2; available at http://cprm.acom.ucar.edu/Models/TUV/). The cloud optical depth value for the TUV model was adjusted so that the predicted UVB radiation intensity matched the observations (Lyu et al., 2019; Wang et al., 2022b). The calculated •OH concentration varied from 0.1 × 10^6 to 4 × 10^6 molecule/cm^3 at U-ZK and 0.1 × 10^6 to 5 × 10^6 molecule/cm^3 t R-PY, which was comparable to the levels in other cities of North China (Li et al., 2018; Fuchs et al., 2017; Yang et al., 2017). Since there is no photolysis at night, the •OH concentration was assumed to be 0.8 × 10^6 molecule/cm^3 (Wang et al., 2022).

6. In the supplement, is the equation (4) utilized in the calculation?

Response: Sorry for the mistake. We have corrected the formula:

$$P_{ground} = \frac{1}{8}\gamma_1\times[NO_2]\times C_{NO_2}\times\frac{S_g}{V} \quad (4)$$

$$P_{aerosol} = \frac{1}{4}\gamma_2\times[NO_2]\times C_{NO_2}\times\frac{S_a}{V} \quad (5)$$

$$\frac{S_g}{V} = \frac{1}{MLH} \quad (6)$$

7. The J_{HONO} and $J_{nitrate}$ used are suggested to be described in detail.

Response: Thanks for your suggestion. We have added a detailed description:

"$J(O^1D)$, $J(NO_2)$, and J(HONO) are the photolysis rates calculated using the TUV model (v5.2; available at http://cprm.acom.ucar.edu/Models/TUV/). The cloud optical depth value for the TUV model was adjusted so that the predicted UVB radiation intensity matched the observations (Lyu et al., 2019; Wang et al., 2022b)."

"The $J_{nitrate \rightarrow HONO}$ was simulated by normalizing UV values when the Zenit Angle is 0°, $J_{nitrate \rightarrow HONO}$ varied within the range of 1.22×10^{-5} to 4.84×10^{-4} s^{-1}, with an average value of 8.24×10^{-5} s^{-1} (Bao et al., 2018)."

Manuscript

Measurement Report: Elevated excess-NH_3 can promote the redox reaction to produce HONO: Insights from the COVID-19 pandemic

Xinyuan Zhang[1,2], Lingling Wang[3], Nan Wang[3], Shuangliang Ma[3], Shenbo Wang[2,4 *], Ruiqin Zhang[2,4**], Dong Zhang[1,2], Mingkai Wang[2,4], Hongyu Zhang[1,2].

[1] College of Chemistry, Zhengzhou University, Zhengzhou, 450000, China

[2] Research Institute of Environmental Sciences, Zhengzhou University, Zhengzhou 450000, China

[3] Henan Provincial Ecological Environment Monitoring and Safety Center, Zhengzhou, 450000, China

[4] School of Ecology and Environment, Zhengzhou University, Zhengzhou, 450000, China

Correspondence: Shenbo Wang (shbwang@zzu.edu.cn) and Ruiqin Zhang (rqzhang@zzu.edu.cn)

Abstract

HONO plays a crucial role as a precursor to OH radicals in the tropospheric atmosphere. The incongruity between HONO concentration and NO_x emissions during the COVID-19 pandemic remains puzzling. Here, we show evidence from field observations of ten sites in China that there was a noticeable increase in NH_3 concentrations during the COVID-19 pandemic. In addition to the meteorological conditions, the significant decrease in sulfate and nitrate concentrations enhanced the portioning of NH_4^+ to NH_3. Such conditions enable enhanced particle pH values, which in turn accelerate the redox reactions between NO_2 and SO_2 to form HONO. This mechanism partly explains the lower reduction of HONO concentration than that of NO_2 concentration during the pandemic and highlights the importance of coordinating the control of SO_2, NO_x, and NH_3 emissions.

Keywords: Ammonia, HONO, Gas-particle portioning, Acidity, COVID-19 pandemic

1. Introduction

Nitrous acid (HONO) is a critical precursor of hydroxyl radical (OH), contributing to more than 60% of OH production (Alicke, 2003; Platt et al., 1980; Kleffmann et al., 2005). The OH can react with carbon monoxide, nitrogen oxides (NO_x), sulfur dioxide (SO_2), and volatile organic compounds to produce secondary pollutants such as ozone (O_3) and $PM_{2.5}$ (particulate matter with an aerodynamic diameter less than or equal to 2.5 μm), thereby affecting air quality, human health, and global climate change (Li et al., 2021a; Wang et al., 2023b; Lu et al., 2018)

High concentrations of HONO are present in urban daytime atmospheres, and exploring its sources has become a hot and challenging topic in the field of atmospheric chemistry (Jiang et al., 2022; Xu et al., 2019). Various sources of atmospheric HONO have been identified, including combustion processes (e.g., vehicle emissions) (Kramer et al., 2020; Liao et al., 2021; Li et al., 2021b), direct emissions from soil (Su and Zhang, 2011; Oswald et al., 2013; Meusel et al., 2018), homogeneous reactions between NO and OH radicals (Pagsberg et al., 1997; Atkinson et al., 2004), heterogeneous reactions of NO_2 on aerosols and ground surfaces (Zhang et al., 2020a; McFall et al., 2018; Liu et al., 2014, 2020a), and photolysis of nitrate (Spataro and Ianniello, 2014; Scharko et al., 2014; Romer et al., 2018; Ye et al., 2017; Shi et al., 2021). During the pandemic control periods, there was a substantial reduction in vehicle traffic flow and industrial emissions, leading to a decrease of more than 60% in NO_x emissions in eastern China (Huang et al., 2021a). It was initially expected that the concentration of HONO would also decrease proportionally. However, Liu et al. (2020b) observed that the decrease in

HONO concentration during the pandemic period was only 31%, which was significantly lower than the reductions in NO (62%) and NO_2 (36%). Furthermore, the observed concentrations of HONO during the COVID-19 pandemic in 2020 were higher than those during the corresponding period in 2021 in Beijing (Luo et al., 2023). These findings suggest the existence of a considerable unknown source of HONO during the COVID-19 pandemic period.

Ammonia (NH_3) is a primary alkaline gas in the atmosphere, capable of influencing the pH level of particulate matter and plays a crucial role in the atmospheric nitrogen cycle (Gu et al., 2022; Xu et al., 2020; Gong et al., 2011). Several studies have indicated that NH_3 can promote the formation of HONO by promoting the hydrolysis of NO_2 (Xu et al., 2019) or the redox reaction of NO_2 with SO_2 (Liu et al., 2023). Moreover, previous studies have reported that NH_3 concentrations in the atmosphere, particularly in rural areas, significantly increased during the pandemic (Xu et al., 2022; Cui, 2023; Zhang et al., 2020b). Consequently, the rise in NH_3 may contribute to the enhanced formation of HONO (Huang et al., 2021a). Unfortunately, there is currently a lack of research on the relationship between enhanced NH_3 and HONO during the COVID-19 pandemic period.

To address this, online observational data on the chemical composition of $PM_{2.5}$, gaseous pollutants, and meteorological conditions at ten sites in China before and during the COVID-19 pandemic period were analyzed to investigate the variation in NH_3 concentrations and particle pH, and explore the promoting effect of increased pH values on HONO formation.

2. Materials and methods

2.1 Observation sites

Online measurements were conducted at four urban and six rural sites in Henan Province, China from January 1 to February 29, 2020, including Sanmenxia (U-SMX), Zhoukou (U-ZK), Zhumadian (U-ZMD), and Xinyang (U-XY), as well as rural locations including Anyang (R-AY), Xinxiang (R-XX), Jiaozuo (R-JZ), Shangqiu (R-SQ), Nanyang (R-NY), and Puyang (R-PY). Descriptions and the spatial distribution of these ten sites can be found in Table S1 and Fig. S1.

2.2 Measurements

The aerosol and gas monitor (MARGA, Metrohm, Switzerland) was used to analyze the hourly water-soluble ions (Na^+, NH_4^+, K^+, Mg^{2+}, Ca^{2+}, Cl^-, NO_3^-, and SO_4^{2-}) in $PM_{2.5}$, as well as gaseous species (NH_3, HNO_3, HCl, and HONO) at ten sampling sites. The MARGA instrument is widely used (Chen et al., 2017; Stieger et al., 2019; Twigg et al., 2022). A detailed description of the instrument and QA/QC can be found in Text S1. In brief, the atmospheric sample passes through a $PM_{2.5}$ cut-off head, and both particles and gases enter a wet rotating dissolution device for diffusion. Subsequently, the particles in the sample undergo hygroscopic growth and condensation in an aerosol supersaturated vapor generator, followed by collection and ion chromatographic analysis. The gases in the sample are oxidized by H_2O_2 in the dissolution device, absorbed into a liquid solvent, and then entered the gas sample collection chamber for

ion chromatographic quantification. The range of minimum detection limits for water-soluble ions was between 0.002 μg/m^3 (Cl^-) to 0.081 μg/m^3 (NH_4^+). Uncertainties of 20% are assumed for the detection of NH_3 and NH_4^+, while uncertainties of 10% are assumed for other components (Wang et al., 2020, 2022a). In addition, a detailed description of HONO measurement using this system can be found in Text S2. Overall, the limit of detection for HONO was 4 pptv and the uncertainty was estimated to be ± 20%.

The data for NO_2 and SO_2 were obtained from a series of instruments provided by Thermo Fisher Scientific (USA). The hourly concentrations of organic carbon (OC) in $PM_{2.5}$ were analyzed using a carbon analyzer (Model 4, Sunset Laboratory., USA). Detailed descriptions of the NO_2, SO_2, and carbon analyzers can be found in Text S3. The smart weather stations (LUFFTWS500, Sutron, Germany) were utilized for synchronized observation of meteorological parameters including pressure, temperature (T), and relative humidity (RH).

2.3 Data analysis.

2.3.1 pH prediction.

The thermodynamic model ISORROPIA-II was used to estimate the pH value of the particles (Fountoukis, 2007) by inputting RH, T, K^+, Ca^{2+}, Mg^{2+}, total ammonia ($TNH_x = 17 \times (\frac{[NH_4^+]}{18} + \frac{[NH_3]}{17})$), total sulfuric acid ($TH_2SO_4$, SO_4^{2-}), total sodium (TNa, Na^+), total chlorine (TCl, Cl^-), and total nitrate ($TNO_3 = NO_3^- + HNO_3$). The model has two calculation modes: the forward mode and reverse mode, and the aerosol

dissolution systems can be set to simulate a metastable state (aqueous phase) or stable state (aqueous and solid phase). Studies have shown that the forward mode is less affected by instrument measurement errors than the reverse mode (Ding et al., 2019; Song et al., 2018). Additionally, the minimum average RH of about 55% was recorded during the sampling period at the ten sites. Thus, ISORROPIA-II was run in the forward model for the aerosol system in the metastable condition and only used data with RH ≥ 30% for simulation accuracy (Ding et al., 2019; Song et al., 2018). The ISORROPIA model calculated the particle hydrate ion concentration per volume of air (H_{air}^{+}) and aerosol water associated with inorganic matter (AWC_{inorg}). The pH value was calculated using the following equation (Bougiatioti et al., 2016):

$$pH = -\log_{10}H_{aq}^{+} = -\log_{10}\frac{1000H_{air}^{+}}{AWC_{inorg} + AWC_{org}} \quad (2.1)$$

where the modeled concentrations for AWC_{inorg} and H_{air}^{+} are μg/m^3, and AWC_{org} is the particle water associated with the organic matters predicted using the following method:

$$AWC_{org} = \frac{m_s}{\rho_s}\frac{k_{org}}{\left(\frac{1}{RH} - 1\right)} \quad (2.2)$$

where m_s is the mass concentration of organic matter (OM = OC × f). The f is the conversion factor of OC, which is dependent on the extent of OM oxidation and secondary organic aerosol formation (Chow et al., 2015). Studies on the ratio of OM/OC in fourteen cities in China suggested that the mean value of f was 1.59 ± 0.18 during the winter season in Northern China (Xing et al., 2013), and thus we adopted 1.6 as the f in this study. k_{org} is the organic hygroscopicity parameter and depends on organic functionality, water solubility, molecular weight, and oxidation level. Han et al. (2022)

have reported that the k_{org} generally increased with O: C ratios, with a range of 0–0.3 for 23 organics, including carboxylic acids, amino acids, sugars, and alcohols. Gunthe et al, (2011) estimated a k_{org} = 0.06 ± 0.01 for the effective average hygroscopicity of the non-refractory organic particulate matter in the aerosols in Beijing. Our previous study has estimated that the uncertainties of k_{org} value (0.06) for pH in the range of 0–0.3 only lead to –1–3% errors, which can be neglected (Wang et al., 2023a). Therefore, the value of 0.06 was selected in this paper. ρ_s is the organic density, which was chosen to be 1.35 g/cm^3 following previous studies (Table S2).

2.3.2 The sources of HONO

The sources of HONO include direct emission (P_{emi}), the homogeneous reaction of NO and •OH (P_{OH+NO}), the heterogeneous reaction of NO_2 on the ground (P_{ground}) and aerosol ($P_{aerosol}$), the photo-enhanced heterogeneous reaction of NO_2 on the ground ($P_{ground+hv}$) and aerosol ($P_{aerosol+hv}$), and nitrate photolysis ($P_{nitrate}$). The detailed calculation method is described in the Supplementary Material (Text S4, Table S3, Figs. S2 and S3)

2.3.3 Redox reaction of NO_2 with SO_2.

The redox reaction of NO_2 with SO_2 (R_1) is considered a crucial potential source of high concentrations of HONO in Northern China (Cheng et al., 2019; Wang et al., 2016b):

$$S(IV) + 2NO_2 + H_2O \rightarrow S(VI) + 2H^+ + 2NO_2^- \quad (R_1)$$

the rate expression for reaction (R_1) was estimated to:

$$d[S(VI)] / dt = k_1[NO_2][S(VI)], \quad (2.3)$$

the rate constant k_1 value is pH dependent, e.g., for pH, 5, $k_1 = (1.4\times10^5+1.24\times10^7)/2$ M^{-1} s^{-1}. For k_1 values under other pH conditions and other related information, please refer to Text S5, Table S4, and Table S5.

3. Results and discussion

3.1 Variations of NH_3, NH_4^+ and TNH_x.

The temporal variations of NH_3, NH_4^+, and TNH_x at 10 sampling sites in the pre-COVID-19 pandemic period (PC, January 1 to 23, 2020) and during the COVID-19 pandemic period (DC, January 24 to February 29, 2020) are presented in Fig. 1, with their average concentration listed in Table 1. In general, rural sites exhibited higher concentrations of NH_3, NH_4^+, and TNH_x compared to urban sites, except for the R-NY site. This finding is consistent with previous studies conducted in Zhengzhou (Wang et al., 2020), Shanghai (Chang et al., 2019), and Quzhou (Feng et al., 2022a), owing to the intense agricultural ammonia emissions. The highest concentrations of NH_3 and TNH_x were recorded at site R-JZ, with average values of 25.3 ± 11.5 and 40.8 ± 20.1 μg/m^3, respectively. Site R-AY had the highest NH_4^+ concentration, measuring 19.3 ± 12.9 μg/m^3. Note that the current study area exhibited higher NH_3 levels compared to other regions (Table S6), which probably was attributed to the highest NH_3 emissions of Henan Province in China, primarily from nitrogen fertilizer application and livestock farming (Wang et al., 2018; Ma, 2020).

Compared to the PC, NH_3 concentrations increased in the DC at all sites. Notably, rural sites experienced more significant increases in NH_3 concentrations than urban sites, which was similar to the trend in Shanghai (Xu et al., 2022). The largest increases in NH_3 concentrations were observed at R-SQ (71%, 7.3 μg/m^3) and U-ZK (37%, 4.8 μg/m^3) for rural and urban sites, respectively. In contrast, the concentrations of NH_4^+ and TNH_x decreased in the DC with the largest reduction at rural site R-PY (51%, 12.9 μg/m^3) and urban site U-ZMD (48%, 9.3 μg/m^3). Regarding TNH_x, rural sites exhibited larger reductions, with site R-SQ experiencing the largest decrease of 37% (4.7 μg/m^3).

Figure 2 illustrates the spatial distribution and the diurnal variation of NH_3 concentrations at the ten sites before and during the pandemic. NH_3 concentrations in most sites exhibited an unimodal trend in PC that NH_3 concentrations gradually increased after sunrise, reaching a peak around noon (11:00–12:00), and then decreased to a valley around 16:00–17:00. This diurnal pattern is similar to NH_3 variations observed in urban areas of Houston, USA, as a result of the natural emissions from vegetation and soil during photosynthesis (Gong et al., 2011). However, other studies have recorded a significant NH_3 peak during the early morning of 8:00–10:00 (Ellis et al., 2011; Meng et al., 2018; Gu et al., 2022), suggesting the influence of vehicle emissions (Gong et al., 2011; Gu et al., 2022), residual NH_3 mixing, soil or plant emissions (Ellis et al., 2011), and dew volatilization (Wentworth et al., 2016; Huang et al., 2021b). Therefore, the NH_3 in urban and rural areas of this study was probably less affected by NH_3 emissions from vehicles, different from the recent studies in megacities of China (e.g., Beijing and Shanghai) (Gu et al., 2022; Wu et al., 2023; Zhang et al.,

2020b). In addition to the transport from agricultural emissions, urban NH_3 in this region might also originate from other non-agricultural sources, such as wastewater treatment, coal combustion, household waste, urban green spaces, and human excrement (Chang et al., 2019).

During the COVID-19 pandemic, the diurnal variation of NH_3 in both urban and rural sites still maintained an unimodal distribution. The peak values in urban sites remained consistent with PC levels, further demonstrating that the influence of vehicles on NH_3 in urban areas was limited. Notably, the peak time of NH_3 in rural sites shifted 1–2 hours earlier compared to the trend in PC. Ammonia in rural areas primarily originates from nitrogen fertilizer application, livestock, and poultry breeding (Feng et al., 2022b; Meng et al., 2018), which are significantly influenced by T and RH (Liu et al., 2023). Table S7 and Fig. S4 reveal that there was an increased T and a decreased RH at rural sites in the DC than the PC, which could accelerate the evaporation of NH_3 and thus potentially lead to earlier peak NH_3 concentrations.

3.2 Gas-to-particle conversion of NH_3

The increased NH_3 accompanying decreased NH_4^+ in the DC suggests that the gas-particle partition of NH_3/ NH_4^+ may determine the elevated NH_3 concentrations. Meteorological parameters, including RH and T, play a crucial role in the gas-particle partitioning of NH_3 (Liu et al., 2023; Xu et al., 2020). Therefore, the higher T and lower RH in the DC (Table S7 and Fig. S4) favored the conversion of NH_4^+ to NH_3, resulting in a decrease in $\varepsilon(NH_4^+)$ ($[NH_4^+]/([NH_3] + [NH_4^+])$ compared to those in the PC (Table

S7).

NH_3 primarily enters particles to neutralize acidic ions (Wang et al., 2020; Xu et al., 2020; Liu et al., 2017; Ye et al., 2011; Wells, 1998). Accordingly, the concentrations of required ammonia (Required-NH_x) and excess ammonia (Excess-NH_x) were calculated based on the acidic substances as follows (Wang et al., 2020):

$$\begin{aligned}\text{Required-NH}_x = 17 \times \left(\frac{[SO_4^{2-}]}{48} + \frac{[NO_3^-]}{63} + \frac{[Cl^-]}{35.5} + \frac{[HNO_3]}{64} + \frac{[HCl]}{36.5}\right) \\ - 17 \times \left(\frac{[Na^+]}{23} + \frac{[K^+]}{39} + \frac{[Ca^{2+}]}{20} + \frac{[Mg^{2+}]}{12}\right)\end{aligned} \quad (3.1)$$

$$\text{Excess-NH}_x = \text{TNH}_x - \text{Required-NH}_x \quad (3.2)$$

where [W] represents the concentration of the substance ($\mu g/m^3$). The significant linear fitting (R^2 is greater than 0.96, and the slope is close to 1) in Fig. S5 demonstrates that the anions and cations at each site were close to the equilibrium state. Therefore, the organic acids in $PM_{2.5}$ may have less effect on NH_3 and NH_4^+ and were not considered in Formula 3.1.

As shown in Fig. 3 and Table S8, compared to those in the PC, the concentration of Required-NH_x in the DC significantly decreased (ranging from 37% at site R-JZ to 58% at site R-PY), while the concentration of Excess-NH_x increased (ranging from 9% at site R-AY to 78% at site R-SQ). The reduction in the concentrations of sulfate and nitrate (Fig. S6) was responsible for the decrease in the concentration of Required-NH_x. To sum up, in addition to meteorological conditions, the substantial reduction in anthropogenic emissions of SO_2, NO_x, and other pollutants in the DC had led to a decrease in acidic substances (e.g., sulfate and nitrate) in particles, in turn, resulting in more gas-phase NH_3 concentration remaining in the atmosphere.

3.3 Particle pH before and during COVID-19

Diurnal patterns of particle pH in PC and DC at ten sites are summarized in Fig. 4 with their average values listed in Table S9. $PM_{2.5}$ shows consistent moderate acidity, with mean values in the range of 4.2–5.1, which were close to the values in previous studies (Table S9). Compared to the PC, the particle pH at ten sites increased obviously in the DC, with the highest increase of 0.5 (U-ZK) and 0.3 (R-PY) at urban and rural sites, respectively, which were the subject of in-depth discussion in the following text.

To explore the dominant factors that determine the local particle pH level and result in the high pH during the DC, sensitivity tests of pH to chemical species (i.e., TNH_x, TH_2SO_4, TNO_3, TCl, TNa, K^+, Ca^{2+}, and Mg^{2+}) and meteorological parameters (i.e., T and RH) were performed. A given range for a variable (i.e., TNH_x) with corresponding average values of other parameters (i.e., TH_2SO_4, TNO_3, TCl, TNa, K^+, Ca^{2+}, Mg^{2+}, T, and RH) was input into the model and simulated to compare its effects on pH. As shown in Fig. S7, pH increases with the cation concentrations (i.e., TNH_x, Na^+, K^+, Ca^{2+}, and Mg^{2+}) increasing as well as the anion concentrations (i.e., TH_2SO_4, TNO_3, and Cl^-), T and RH decreasing. According to the average values of input data during PC (Blue line in Fig. S7) and DC (Red line in Fig. S7) at U-ZK and R-PY sites respectively, the changes in pH (ΔpH in Fig. 5) indicate that the decrease in TNH_x concentration and the increase in T in DC led to a decrease in pH values (ΔpH: 0.09 at U-ZK and 0.08 at R-PY sites) compared to PC. However, this effect was outweighed by the decrease in TH_2SO_4 (ΔpH: 0.07 and 0.8 at U-ZK and R-PY sites, respectively) and TNO_3 (ΔpH: 0.05 and 0.4 at U-ZK and R-PY sites, respectively) concentrations as well as the

increase in K^+ (ΔpH: 0.03 at U-ZK and 0.2 at R-PY site) and Mg^{2+} (ΔpH: 0.01 at U-ZK and 0.04 at R-PY site) concentrations in the DC, and resulting in an overall increase in pH values in the DC. Furthermore, the relationship between particle pH with the concentrations of Required-NH_x, and Excess-NH_x, which considers all chemical components, is investigated to examine the dominant factor on the increasing pH in DC. As shown in Fig. 6, the higher Excess-NH_x concentrations in the DC led to higher increases in pH values (ΔpH: 1 at U-ZK and 0.5 at R-PY site) than those in PC (ΔpH: 0.3 at U-ZK and 0.2 at R-PY site), thus Excess-NHx concentrations may be the key factor in promoting the pH values.

3.4 The influence of pH on HONO.

The observed HONO concentrations decreased by 18% and 54% at U-ZK (0.8 ppb) and R-PY (0.9 ppb) sites in the DC, respectively, compared to those (1.0 and 2.2 ppb) in the PC. Moreover, all the known HONO production sources rates including P_{emi}, P_{OH+NO}, P_{ground}, $P_{ground+hv}$, $P_{aerosol}$, $P_{aerosol+hv}$, and $P_{nitrate}$ (Fig. 7) show a decreasing trend from PC to DC, with the total reductions of 42% and 80% for U-ZK and R-PY, respectively. At the U-ZK, $P_{ground+hv}$ decreased the most (84%), while at the R-PY, $P_{nitrate}$ had the largest decrease about 85%, which was speculated to be related to the decrease of NO_x and NO_3^- concentration in DC. Note that the reduction rates in the overall known source and almost individual sources were greater than the reduction rates in HONO concentrations (Figs. 7 and 8), thus we hypothesized that there should be other sources capable of promoting HONO production. Soil emission has been demonstrated to be a

major source of HONO, which is affected by temperature to some extent (Liu et al., 2020b, 2020c). However, there was no significant positive correlation with temperature in Fig. S8, and temperatures did not exceed 10°C during the study periods, suggesting that soil emission may not be a major contributor to HONO. Note that there were positive correlations between HONO with SO_2, Excess-NH_x, SO_4^{2-}, and pH (Fig. S8) indicating that the R_1 reaction might form an amount of HONO and contribute to less reduction in the observed HONO concentrations.

Considering that R_1 mainly reacts in the liquid phase, the calculated reaction rates of R_1 under the conditions of RH > 60% in the PC and DC periods are illustrated in Figs. 8 and S9. Despite the decrease in NO_2 and SO_2 concentrations in the DC, the increase in particle pH, increasing HSO_3^- concentration in the aqueous phase, promoted the R_1 reaction rates by 58% and 59% at U-ZK and R-PY (Figure 8), respectively. Consequently, the enhanced R_1 reaction might prevent a large decrease in HONO (18% at U-ZK and 53% at R-PY) under the conditions of a significant reduction in vehicle emissions and a decline of 66% and 69% in NO_2 concentrations at U-ZK and R-PY, respectively.

3.5 Uncertainty

According to sensitivity tests of pH (Fig. S7) and R_1 (Fig. S10), pH increases with the concentrations of cations (TNH_x, TNa, K^+, Ca^{2+}, and Mg^{2+}) and OC increasing as well as anions (TH_2SO_4, TNO_3, and Cl^-) concentrations, T, and RH decreasing. R_1 reaction rate increases with the concentrations of AWC, NO_2, SO_2, pH, and pressure,

while increasing as well as T decreasing. Therefore, two extreme scenarios (i.e., the maximum and minimum rate scenarios) were evaluated to estimate the uncertainty of pH, and R_1 based on the measurement uncertainties at the U-ZK and R-PY sites. Figure S11 suggests that the two extreme scenarios can be led to –10–7% and –71–125% uncertainties at the U-ZK site and –10–7% and –78–123% uncertainties at the R-PY site for pH and R_1, respectively.

4. Conclusions

Elevated NH_3 concentration was observed during the COVID-19 pandemic at both urban and rural sites in China. In addition to the rise in T and decrease in RH during the COVID-19 pandemic, which favored the conversion of NH_4^+ to NH_3, the significant decrease in sulfate and nitrate concentrations led to the decline in Required-NH_x and was beneficial to the particle-phase NH_4^+ portioning to gas-phase NH_3. Furthermore, under the environmental conditions of increased NH_3 concentration and decreased acidic substance concentration, the pH values increased by 0.5 and 0.3 at U-ZK and R-PY increased during the pandemic, respectively. Consequently, the high pH values accelerated the formation rate of HONO through the oxidation-reduction reaction of NO_2 with SO_2 (an increase of 58% at U-ZK and 59% at R-PY, respectively), partially compensating for the decrease in HONO concentration caused by the decline in vehicle emissions, NO_2 and NO_3^- concentrations during the COVID-19 pandemic.

5. Implications

HONO plays a crucial role as a precursor to OH radicals in the tropospheric atmosphere (Xue, 2022). There have been significant observations of high HONO concentrations in urban areas during the daytime, leading to a growing interest in understanding its sources in atmospheric chemistry (Jiang et al., 2022; Xu et al., 2019). The heterogeneous reaction mechanism of NO_2 on aerosol surfaces is currently the focus of research on HONO sources, particularly in regions with elevated levels of atmospheric particulate matter, where it could potentially become a major contributor to HONO production (Zhang et al., 2022; Liao et al., 2021). One of the pathways for heterogeneous reactions on aerosol surfaces is the redox reaction of NO_2 with SO_2. However, the significance of this reaction in HONO production in the real atmosphere is often overlooked, as it relies on the high pH of aerosols (Ge et al., 2019). In recent years, there has been increasing attention on the enhancing effect of NH_3 on the redox reaction, with laboratory experiments demonstrating its ability to generate substantial amounts of HONO (Ge et al., 2019). This study highlights the importance of this reaction based on actual atmospheric observations. Furthermore, numerous studies have indicated that if control over NH_3 emissions continues to relax while SO_2 and NO_2 emissions decrease, the particle pH in future China is expected to rise steadily (Xie et al., 2020; Song et al., 2019; Wang et al., 2020). Consequently, the redox reaction of NO_2 with SO_2 could become a significant source of HONO in China. Therefore, it is crucial to coordinate the control of SO_2, NO_x, and NH_3 emissions to avoid a rapid increase in the particle pH.

Data availability: All the data presented in this article can be accessed through https://zenodo.org/records/10273539. (Zhang, 2023).

Author contributions. XZ Data Curation, Writing - Original Draft, Visualization. LW, NW, SM, and DZ Investigation, Visualization, Data Curation. DZ, HZ, and MW Investigation. SW Conceptualization, Data Curation, Supervision. RZ Data Curation, Funding acquisition. All people are involved in the discussion of the results.

Competing interest. The authors declare no competing financial interest.

Acknowledgments. This work was supported by the China Postdoctoral Science Foundation (2023M733220), the Zhengzhou $PM_{2.5}$ and O_3 Collaborative Control and Monitoring Project (20220347A), and the National Key Research and Development Program of China (No. 2017YFC0212403).

References

Alicke, B.: OH formation by HONO photolysis during the BERLIOZ experiment, J. Geophy. Res.; 108, 8247, https://doi.org/10.1029/2001JD000579, 2003.

Atkinson, R., Baulch, D.L., Cox, R.A., Crowley, J.N., Hampson, R.F., Hynes, R.G., Jenkin, M.E., and Rossi, M. J., Troe, J.: Evaluated kinetic and photochemical data for atmospheric chemistry: volume I - gas phase reactions of O_x, HO_x, NO_x and SO_x species., Atmos. Chem. Phys., 4,1461–1738, https://doi.org/10.5194/acp-4-1461-2004, 2004.

Bougiatioti, A., Nikolaou, P., Stavroulas, I., Kouvarakis, G., Weber, R., Nenes, A., Kanakidou, M., and Mihalopoulos, N.: Particle water and pH in the eastern Mediterranean: source variability and implications for nutrient availability, Atmos. Chem. Phys., 16, 4579–4591, https://doi.org/10.5194/acp-16-4579-2016, 2016.

Chang, Y., Zou, Z., Zhang, Y., Deng, C., Hu, J., Shi, Z., Dore, A. J., and Collett, J. L., Jr.: Assessing contributions of agricultural and nonagricultural emissions to atmospheric ammonia in a Chinese megacity. Environ. Sci. Technol. 53, 1822–1833., https://doi.org/10.1021/acs.est.8b05984, 2019.

Chen, X., Walker, J. T., and Geron, C.: Chromatography related performance of the monitor for aerosols and gases in ambient air (MARGA): laboratory and field-based evaluation. Atmos. Meas. Tech. 10, 3893–3908. https://doi.org/10.5194/amt-10-3893-2017, 2017.

Cheng, Y., Zheng, G., Wei, C., Mu, Q., Zheng, B., Wang, Z., Gao, M., Z., Q., He, K., Carmichael, G., Pöschl, U., and Su, and H.: Reactive nitrogen chemistry in aerosol

water as a source of sulfate during haze events in China, Sci. Adv. 2, e1601530., https://doi.org/10.1126/sciadv.1601530, 2019.

Chow, J. C., Lowenthal, D. H., Chen, L. W. A., Wang, X., and Watson, J. G.: Mass reconstruction methods for $PM_{2.5}$: a review, Air Qual. Atmos. Health., 8, 243 – 263, https://doi.org/10.1007/s11869-015-0338-3, 2015.

Cui, L.: Impact of COVID-19 restrictions on the concentration and source apportionment of atmospheric ammonia (NH_3) across India, Sci. Total Environ., 881, https://doi.org/10.1016/j.scitotenv.2023.163443, 2023.

Ding, J., Zhao, P., Su, J., Dong, Q., Du, X., and Zhang, Y.: Aerosol pH and its driving factors in Beijing, Atmos. Chem. Phys. 19, 7939–7954., https://doi.org/10.5194/acp-19-7939-2019, 2019.

Ellis, R. A., Murphy, J. G., Markovic, M. Z., VandenBoer, T. C., Makar, P. A., Brook, J., and Mihele, C.: The influence of gas-particle partitioning and surface-atmosphere exchange on ammonia during BAQS-Met, Atmos. Chem. Phys. 11, 133–145., https://doi.org/10.5194/acp-11-133-2011, 2011.

Feng, S., Xu, W., Cheng, M., Ma, Y., Wu, L., Kang, J., Wang, K., Tang, A., Collett, J. L., Fang, Y., Goulding, K., Liu, X., and Zhang, F.: Overlooked nonagricultural and wintertime agricultural NH_3 emissions in Quzhou county, north China plain: evidence from ^{15}N-Stable Isotopes. Environ. Sci. Technol. Lett. 9, 127–133, https://doi.org/10.1021/acs.estlett.1c00935, 2022a.

Feng, T., Zhao, S., Liu, L., Long, X., Gao, C., and Wu, N.: Nitrous acid emission from soil bacteria and related environmental effect over the North China Plain, Chemos., 287, https://doi.org/10.1016/j.chemosphere.2021.132034, 2022b.

Fountoukis, C., Nenes, A.: ISORROPIA II: a computationally efficient thermodynamic

equilibrium model for K^+-Ca^{2+}-Mg^{2+}-NH_4^+-Na^+-SO_4^{2-}-NO^{3-}-Cl^--H_2O aerosols. Atmos. Chem. Phys. 7, 4639–4659, https://doi.org/10.5194/acp-7-4639-2007, 2007.

Ge, S., Wang, G., Zhang, S., Li, D., and Zhang, H.: Abundant NH_3 in China enhances atmospheric HONO production by promoting the heterogeneous reaction of SO_2 with NO_2. Environ. Sci. Technol. 53, 14339–14347, https://doi.org/10.1021/acs.est.9b04196, 2019.

Gong, L., Lewicki, R., Griffin, R. J., Flynn, J. H., Lefer, B. L., and Tittel, F. K.: Atmospheric ammonia measurements in Houston, TX using an external-cavity quantum cascade laser-based sensor, Atmos. Chem. Phys. 11, 9721–9733, https://doi.org/10.5194/acp-11-9721-2011, 2011.

Gu, M., Pan, Y., Walters, W. W., Sun, Q., Song, L., Wang, Y., Xue, Y., and Fang, Y.: ehicular emissions enhanced ammonia concentrations in winter mornings: insights from diurnal nitrogen isotopic signatures. Environ. Sci. Technol. 56, 1578–1585, https://doi.org/10.1021/acs.est.1c05884, 2022.

Gunthe, S. S., Rose, D., Su, H., Garland, R. M., Achtert, P., Nowak, A., Wiedensohler, A., Kuwata, M., Takegawa, N., Kondo, Y., Hu, M., Shao, M., Zhu, T., Andreae, M. O., and Pöschl, U.: Cloud condensation nuclei (CCN) from fresh and aged air pollution in the megacity region of Beijing, Atmos. Chem. Phys., 11, 11023 – 11039, https://doi.org/10.5194/acp-11-11023-2011, 2011.

Han, S., Hong, J., Luo, Q., Xu, H., Tan, H., Wang, Q., Tao, J., Zhou, Y., Peng, L., He, Y., Shi, J., Ma, N., Cheng, Y., and Su, H.: Hygroscopicity of organic compounds as a function of organic functionality, water solubility, molecular weight, and

433 oxidation level, Atmos. Chem. Phys., 22, 3985–4004, https://doi.org/10.5194/acp-
434 22-3985-2022, 2022.
435 Huang, X., Ding, A., Gao, J., Zheng, B., Zhou, D., Qi, X., Tang, R., Wang, J., Ren, C.,
436 Nie, W., Chi, X., Xu, Z., Chen, L., Li, Y., Che, F., Pang, N., Wang, H., Tong, D.,
437 Qin, W., Cheng, W., Liu, W., Fu, Q., Liu, B., Chai, F., Davis, S. J., Zhang, Q., and
438 He, K.: Enhanced secondary pollution offset reduction of primary emissions
439 during COVID-19 lockdown in China, Natl Sci Rev, 8, nwaa137,
440 https://doi.org/10.1093/nsr/nwaa137, 2021a.
441 Huang, X., Zhang, J., Zhang, W., Tang, G., and Wang, Y.: Atmospheric ammonia and
442 its effect on $PM_{2.5}$ pollution in urban Chengdu, Sichuan Basin, China. Environ.
443 Pollut. 291, 118–195. https://doi.org/10.1016/j.envpol.2021.118195, 2021b.
444 Jiang, Y., Xue, L., Shen, H., Dong, C., Xiao, Z., and Wang, W.: Dominant processes of
445 HONO derived from multiple field observations in contrasting environments.
446 Environ. Sci. Technol. Lett. 9, 258–264,
447 https://doi.org/10.1021/acs.estlett.2c00004, 2022.
448 Kleffmann, J., Gavriloaiei, T., Hofzumahaus, A., Holland, F., Koppmann, R., Rupp, L.,
449 Schlosser, E., Siese, M., and Wahner, A.: Daytime formation of nitrous acid: A
450 major source of OH radicals in a forest, Geophys. Res. Lett., 32,
451 https://doi.org/10.1029/2005gl022524, 2005.
452 Kramer, L. J., Crilley, L. R., Adams, T. J., Ball, S. M., Pope, F. D., and Bloss, W. J.:
453 Nitrous acid (HONO) emissions under real-world driving conditions from vehicles
454 in a UK road tunnel, Atmos. Chem. Phys. 20, 5231–5248,

https://doi.org/10.5194/acp-20-5231-2020, 2020.

Li, J., An, X., Cui, M., Sun, Z., Wang, C., and Li, Y.: Simulation study on regional atmospheric oxidation capacity and precursor sensitivity, Atmos. Environ. 263, 118657, https://doi.org/10.1016/j.atmosenv.2021.118657, 2021a.

Li, S., Song, W., Zhan, H., Zhang, Y., Zhang, X., Li, W., Tong, S., Pei, C., Wang, Y., Chen, Y., Huang, Z., Zhang, R., Zhu, M., Fang, H., Wu, Z., Wang, J., Luo, S., Fu, X., Xiao, S., Huang, X., Zeng, J., Zhang, H., Chen, D., Gligorovski, S., Ge, M., George, C., and Wang, X.: Contribution of vehicle emission and NO_2 surface conversion to nitrous acid (HONO) in urban environments: implications from tests in a tunnel. Environ. Sci. Technol., 55, 15616–15624, https://doi.org/10.1021/acs.est.1c00405, 2021.

Liao, S., Zhang, J., Yu, F., Zhu, M., Liu, J., Ou, J., Dong, H., Sha, Q., Zhong, Z., Xie, Y., Luo, H., Zhang, L., and Zheng, J.: High gaseous nitrous acid (HONO) emissions from light-duty diesel vehicles. Environ. Sci. Technol. 55, 200–208, https://doi.org/10.1021/acs.est.0c05599, 2021.

Liu, J., Deng, H., Lakey, P. S. J., Jiang, H., Mekic, M., Wang, X., Shiraiwa, M., and Gligorovski, S.: Unexpectedly high indoor HONO concentrations associated with photochemical NO_2 transformation on glass windows. Environ. Sci. Technol. 54, 15680–15688, https://doi.org/10.1021/acs.est.0c05624, 2020a.

Liu, M., Song, Y., Zhou, T., Xu, Z., Yan, C., Zheng, M., Wu, Z., Hu, M., Wu, Y., and Zhu, T.: Fine particle pH during severe haze episodes in northern China. Geophys. Res. Lett. 44, 5213–5221, https://doi.org/10.1002/2017gl073210, 2017.

Liu, P., Chen, H., Song, Y., Xue, C., Ye, C., Zhao, X., Zhang, C., Liu, J., and Mu, Y.: Atmospheric ammonia in the rural North China Plain during wintertime: variations, sources, and implications for HONO heterogeneous formation. Sci. Total. Environ. 861, 160768, https://doi.org/10.1016/j.scitotenv.2022.160768, 2023.

Liu, Y., Ni, S., Jiang, T., Xing, S., Zhang, Y., Bao, X., Feng, Z., Fan, X., Zhang, L., and Feng, H.: Influence of Chinese New Year overlapping COVID-19 lockdown on HONO sources in Shijiazhuang, Sci. Total Environ., 745, 141025, https://doi.org/10.1016/j.scitotenv.2020.141025, 2020b.

Liu, Y., Zhang, Y., Lian, C., Yan, C., Feng, Z., Zheng, F., Fan, X., Chen, Y., Wang, W., Chu, B., Wang, Y., Cai, J., Du, W., Daellenbach, K. R., Kangasluoma, J., Bianchi, F., Kujansuu, J., Petäjä, T., Wang, X., Hu, B., Wang, Y., Ge, M., He, H., and Kulmala, M.: The promotion effect of nitrous acid on aerosol formation in wintertime in Beijing: The possible contribution of traffic-related emissions, Atmos. Chem. Phys, 20, 13023–13040, https://doi.org/10.5194/acp-20-13023-2020, 2020c.

Liu, Z., Wang, Y., Costabile, F., Amoroso, A., Zhao, C., Huey, L. G., Stickel, R., Liao, J., and Zhu, T.: Evidence of aerosols as a media for rapid daytime HONO production over China, Environ. Sci. Technol., 48, 13023–13040, https://doi.org/10.1021/es504163z, 2014.

Lu, K., Guo, S., Tan, Z., Wang, H., Shang, D., Liu, Y., Li, X., Wu, Z., Hu, M., and Zhang, Y.: Exploring atmospheric free-radical chemistry in China: the self-cleansing capacity and the formation of secondary air pollution, Natl. Sci. Rev., 6,

579-594, https://doi.org/10.1093/nsr/nwy073, 2018.

Luo, L., Bai, X., Lv, Y., Liu, S., Guo, Z., Liu, W., Hao, Y., Sun, Y., Hao, J., Zhang, K., Zhao, H., Lin, S., Zhao, S., Xiao, Y., Yang, J., and Tian, H.: Exploring the driving factors of haze events in Beijing during Chinese New Year holidays in 2020 and 2021 under the influence of COVID-19 pandemic, Sci. Total Environ., 859, 160172, https://doi.org/10.1016/j.scitotenv.2022.160172, 2023.

Ma, S.: High-resolution assessment of ammonia emissions in China: Inventories, driving forces and mitigation, Atmos. Environ., 229, https://doi.org/10.1016/j.atmosenv.2020.117458, 2020.

McFall, A. S., Edwards, K. C., and Anastasio, C.: Nitrate photochemistry at the air-ice interface and in other ice reservoirs, Environ. Sci. Technol., 52, 5710–5717, https://doi.org/10.1021/acs.est.8b00095, 2018.

Meng, Z., Xu, X., Lin, W., Ge, B., Xie, Y., Song, B., Jia, S., Zhang, R., Peng, W., Wang, Y., Cheng, H., Yang, W., and Zhao, H.: Role of ambient ammonia in particulate ammonium formation at a rural site in the North China Plain, Atmos. Chem. Phys., 18, 167–184, https://doi.org/10.5194/acp-18-167-2018, 2018.

Meusel, H., Tamm, A., Kuhn, U., Wu, D., Leifke, A. L., Fiedler, S., Ruckteschler, N., Yordanova, P., Lang-Yona, N., Pöhlker, M., Lelieveld, J., Hoffmann, T., Pöschl, U., Su, H., Weber, B., and Cheng, Y.: Emission of nitrous acid from soil and biological soil crusts represents an important source of HONO in the remote atmosphere in Cyprus, Atmos. Chem. Phys., 18, 799 – 813, https://doi.org/10.5194/acp-18-799-2018, 2018.

Oswald, R., Behrendt, T., Ermel, M., Wu, D., Su, H., Cheng, Y., Breuninger, C., Moravek, A., Mougin, E., Delon, C., Loubet, B., Pommerening-Roser, A., Sorgel,

523 M., Poschl, U., and Hoffmann, T., Andreae, M.O., Meixner, F.X., Trebs, I.: HONO
524 emissions from soil bacteria as a major source of atmospheric reactive nitrogen.,
525 Science. 341, 1233–1235, https://www.science.org/doi/10.1126/science.1242266,
526 2013.
527 Pagsberg, P., Bjergbakke, E., Ratajczak, E., Sillesen, A.: Kinetics of the gas phase
528 reaction OH + NO (+M)$^{-}$ > HONO (+M) and the determination of the UV
529 absorption cross sections of HONO., Chem. Phys. Lett. 272, 383–390,
530 https://doi.org/10.1016/s0009-2614(97)00576-9, 1997.
531 Platt, U., Perner, D., Harris, G. W., Winer, A. M., and Pitts, J. N.: Observations of
532 nitrous acid in an urban atmosphere by differential optical absorption, Nature, 285,
533 312–314, https://doi.org/10.1038/285312a0, 1980.
534 Romer, P. S., Wooldridge, P. J., Crounse, J. D., Kim, M. J., Wennberg, P. O., Dibb, J.
535 E., Scheuer, E., Blake, D. R., Meinardi, S., Brosius, A. L., Thames, A. B., Miller,
536 D. O., Brune, W. H., Hall, S. R., Ryerson, T. B., and Cohen, R. C.: Constraints on
537 aerosol nitrate photolysis as a potential source of HONO and NO_x. Environ. Sci.
538 Technol. 52, 13738–13746, https://doi.org/10.1021/acs.est.8b03861, 2018.
539 Scharko, N. K., Berke, A. E., and Raff, J. D.: Release of nitrous acid and nitrogen
540 dioxide from nitrate photolysis in acidic aqueous solutions, Environ. Sci. Technol.,
541 48, 11991–12001, https://doi.org/10.1021/es503088x, 2014.
542 Shi, Q., Tao, Y., Krechmer, J. E., Heald, C. L., Murphy, J. G., Kroll, J. H., and Ye, Q.:
543 Laboratory investigation of renoxification from the photolysis of inorganic
544 particulate nitrate, Environ. Sci. Technol., 55, 854–861,

https://doi.org/10.1021/acs.est.0c06049, 2021.

Song, S., Gao, M., Xu, W., Shao, J., Shi, G., Wang, S., Wang, Y., Sun, Y., and McElroy, M. B.: Fine-particle pH for Beijing winter haze as inferred from different thermodynamic equilibrium models, Atmos. Chem. Phys., 18, 7423–7438, https://doi.org/10.5194/acp-18-7423-2018, 2018.

Song, S., Nenes, A., Gao, M., Zhang, Y., Liu, P., Shao, J., Ye, D., Xu, W., Lei, L., Sun, Y., Liu, B., Wang, S., and McElroy, M. B.: Thermodynamic modeling suggests declines in water uptake and acidity of inorganic aerosols in Beijing winter haze events during 2014/2015–2018/2019. Environ. Sci. Technol. Lett. 6, 752–760, https://doi.org/10.1021/acs.estlett.9b00621, 2019.

Spataro, F., and Ianniello, A.: Sources of atmospheric nitrous acid: state of the science, current research needs, and future prospects, J. Air. Waste. Manag. Assoc., 64, 1232–1250, https://doi.org/10.1080/10962247.2014.952846, 2014.

Stieger, B., Spindler, G., van Pinxteren, D., Grüner, A., Wallasch, M., and Herrmann, H.: Development of an online-coupled MARGA upgrade for the 2 h interval quantification of low-molecular-weight organic acids in the gas and particle phases, Atmos. Meas. Tech. 12, 281–298, https://doi.org/10.5194/amt-12-281-2019, 2019.

Su, H., Cheng, Y., Oswald, R., Behrendt, T., Trebs, I., Meixner, F.X., Andreae, M.O., Cheng, P., and Zhang, Y., Poschl, U.: Soil nitrite as a source of atmospheric HONO and OH radi cals., Science. 333, 1616–1618, https://doi.org/10.1126/science.1207687, 2011.

Twigg, M. M., Berkhout, A. J. C., Cowan, N., Crunaire, S., Dammers, E., Ebert, V.,

Gaudion, V., Haaima, M., Häni, C., John, L., Jones, M. R., Kamps, B., Kentisbeer, J., Kupper, T., Leeson, S. R., Leuenberger, D., Lüttschwager, N. O. B., Makkonen, U., Martin, N. A., Missler, D., Mounsor, D., Neftel, A., Nelson, C., Nemitz, E., Oudwater, R., Pascale, C., Petit, J.-E., Pogany, A., Redon, N., Sintermann, J., Stephens, A., Sutton, M. A., Tang, Y. S., Zijlmans, R., Braban, C. F., and Niederhauser, B.: Intercomparison of in situ measurements of ambient NH_3: instrument performance and application under field conditions, Atmos. Meas. Tech. 15, 6755–6787, https://doi.org/10.5194/amt-15-6755-2022, 2022.

Wang, C., Yin, S., Bai, L., Zhang, X., Gu, X., Zhang, H., Lu, Q., and Zhang, R.: High-resolution ammonia emission inventories with comprehensive analysis and evaluation in Henan, China, 2006–2016, Atmos. Environ. 193, 11–23, https://doi.org/10.1016/j.atmosenv.2018.08.063, 2018.

Wang, S., Wang, L., Li, Y., Wang, C., Wang, W., Yin, S., and Zhang, R.: Effect of ammonia on fine-particle pH in agricultural regions of China: comparison between urban and rural sites, Atmos. Chem. Phys., 20, 2719–2734, https://doi.org/10.5194/acp-20-2719-2020, 2020.

Wang, S., Wang, L., Fan, X., Wang, N., Ma, S., and Zhang, R.: Formation pathway of secondary inorganic aerosol and its influencing factors in Northern China: Comparison between urban and rural sites, Sci. Total Environ., 840, https://doi.org/10.1016/j.scitotenv.2022.156404, 2022.

Wang, S., Fan, X., Xu, Y., Zhang, R., and Ren, B.: Insight into the non-linear responses of particulate sulfate to reduced SO_2 concentration: A perspective from the

589 aqueous-phase reactions in a megacity in Northern China, Atmos. Res., 290,
590 https://doi.org/10.1016/j.atmosres.2023.106796, 2023a.
591 Wang, W., Wang, S., Xu, J., Zhou, R., Shi, C., and Zhou, B.: Gas-phase ammonia and
592 $PM_{2.5}$ ammonium in a busy traffic area of Nanjing, China, Environ. Sci. Pollut.
593 Res. Int., 23, 1691–1702, https://doi.org/10.1007/s11356-015-5397-3, 2016.
594 Wang, Y., Jin, X., Liu, Z., Wang, G., Tang, G., Lu, K., Hu, B., Wang, S., Li, G., An, X.,
595 Wang, C., Hu, Q., He, L., Zhang, F., and Zhang, Y.: Progress in quantitative
596 research on the relationship between atmospheric oxidation and air quality, J.
597 Environ. Sci., 123, 350–366, https://doi.org/10.1016/j.jes.2022.06.029, 2023b.
598 Wells, M., Choularton, T. W., and Bower, K. N.: A modelling study of the interaction
599 of ammonia with cloud., Atmos. Environ., 32, 359–363,
600 https://doi.org/10.1016/s1352-2310(97)00199-4, 1998.
601 Wentworth, G. R., Murphy, J. G., Benedict, K. B., Bangs, E. J., and Collett Jr, J. L.: The
602 role of dew as a night-time reservoir and morning source for atmospheric ammonia,
603 Atmos. Chem. Phys. 16, 7435–7449, https://doi.org/10.5194/acp-16-7435-2016,
604 2016.
605 Wu, C., Lv, S., Wang, F., Liu, X., Li, J., Liu, L., Zhang, S., Du, W., Liu, S., Zhang, F.,
606 Li, J., Meng, J., and Wang, G.: Ammonia in urban atmosphere can be substantially
607 reduced by vehicle emission control: A case study in Shanghai, China, J. Environ.
608 Sci., 126, 754–760, https://doi.org/10.1016/j.jes.2022.04.043, 2023.
609 Xie, Y., Wang, G., Wang, X., Chen, J., Chen, Y., Tang, G., Wang, L., Ge, S., Xue, G.,
610 Wang, Y., and Gao, J.: Nitrate-dominated PM2.5 and elevation of particle pH

observed in urban Beijing during the winter of 2017. Atmos. Chem. Phys. 20, 5019–5033, https://doi.org/10.5194/acp-20-5019-2020, 2020.

Xing, L., Fu, T. M., Cao, J. J., Lee, S. C., Wang, G. H., Ho, K. F., Cheng, M. C., You, C. F., and Wang, T. J.: Seasonal and spatial variability of the OM/OC mass ratios and high regional correlation between oxalic acid and zinc in Chinese urban organic aerosols, Atmos. Chem. Phys., 13, 4307–4318, https://doi.org/10.5194/acp-13-4307-2013, 2013.

Xu, J., Chen, J., Zhao, N., Wang, G., Yu, G., Li, H., Huo, J., Lin, Y., Fu, Q., Guo, H., Deng, C., Lee, S.-H., Chen, J., and Huang, K.: Importance of gas-particle partitioning of ammonia in haze formation in the rural agricultural environment, Atmos. Chem. Phys. 20, 7259–7269, https://doi.org/10.5194/acp-20-7259-2020, 2020.

Xu, W., Kuang, Y., Zhao, C., Tao, J., Zhao, G., Bian, Y., Yang, W., Yu, Y., Shen, C., Liang, L., Zhang, G., Lin, W., and Xu, X.: NH_3-promoted hydrolysis of NO_2 induces explosive growth in HONO, Atmos. Chem. Phys. 19, 10557–10570, https://doi.org/10.5194/acp-19-10557-2019, 2019.

Xu, W., Zhao, Y., Wen, Z., Chang, Y., Pan, Y., Sun, Y., Ma, X., Sha, Z., Li, Z., Kang, J., Liu, L., Tang, A., Wang, K., Zhang, Y., Guo, Y., Zhang, L., Sheng, L., Zhang, X., Gu, B., Song, Y., Van Damme, M., Clarisse, L., Coheur, P. F., Collett, J. L., Jr., Goulding, K., Zhang, F., He, K., and Liu, X.: Increasing importance of ammonia emission abatement in $PM_{2.5}$ pollution control. Sci. Bull. 67, 1745–1749, https://doi.org/10.1016/j.scib.2022.07.021, 2022.

633 Xue, C.: Substantially growing interest in the chemistry of nitrous acid (HONO) in
634 China: current achievements, problems, and future directions. Environ. Sci.
635 Technol. 56, 7375–7377. https://doi.org/10.1021/acs.est.2c02237, 2022.
636 Ye, C., Zhang, N., Gao, H., and Zhou, X.: Photolysis of particulate nitrate as a source
637 of HONO and NO_x. Environ. Sci. Technol. 51, 6849–6856,
638 https://doi.org/10.1021/acs.est.7b00387, 2017.
639 Ye, X., Ma, Z., Zhang, J., Du, H., Chen, J., Chen, H., Yang, X., Gao, W., and Geng, F.:
640 Important role of ammonia on haze formation in Shanghai, Environ. Res. Lett. 6,
641 024019, https://doi.org/10.1088/1748-9326/6/2/024019, 2011.
642 Zhang, W., Tong, S., Jia, C., Wang, L., Liu, B., Tang, G., Ji, D., Hu, B., Liu, Z., Li, W.,
643 Wang, Z., Liu, Y., Wang, Y., and Ge, M.: Different HONO sources for three layers
644 at the urban area of Beijing. Environ. Sci. Technol. 54, 12870–12880,
645 https://doi.org/10.1021/acs.est.0c02146, 2020a.
646 Zhang, W., Tong, S., Jia, C., Ge, M., Ji, D., Zhang, C., Liu, P., Zhao, X., Mu, Y., Hu, B.,
647 Wang, L., Tang, G., Li, X., Li, W., and Wang, Z.: Effect of different combustion
648 processes on atmospheric nitrous acid formation mechanisms: a winter
649 comparative observation in urban, suburban and rural areas of the North China
650 Plain. Environ. Sci. Technol. 56, 4828–4837,
651 https://doi.org/10.1021/acs.est.1c07784, 2022.
652 Zhang, Y., Liu, X., Fang, Y., Liu, D., Tang, A., and Collett, J. L.: Atmospheric ammonia
653 in Beijing during the COVID-19 outbreak: concentrations, sources, and
654 implications. Environ. Sci. Technol. Lett. 8, 32–38,

https://doi.org/10.1021/acs.estlett.0c00756, 2020b.

Figures:

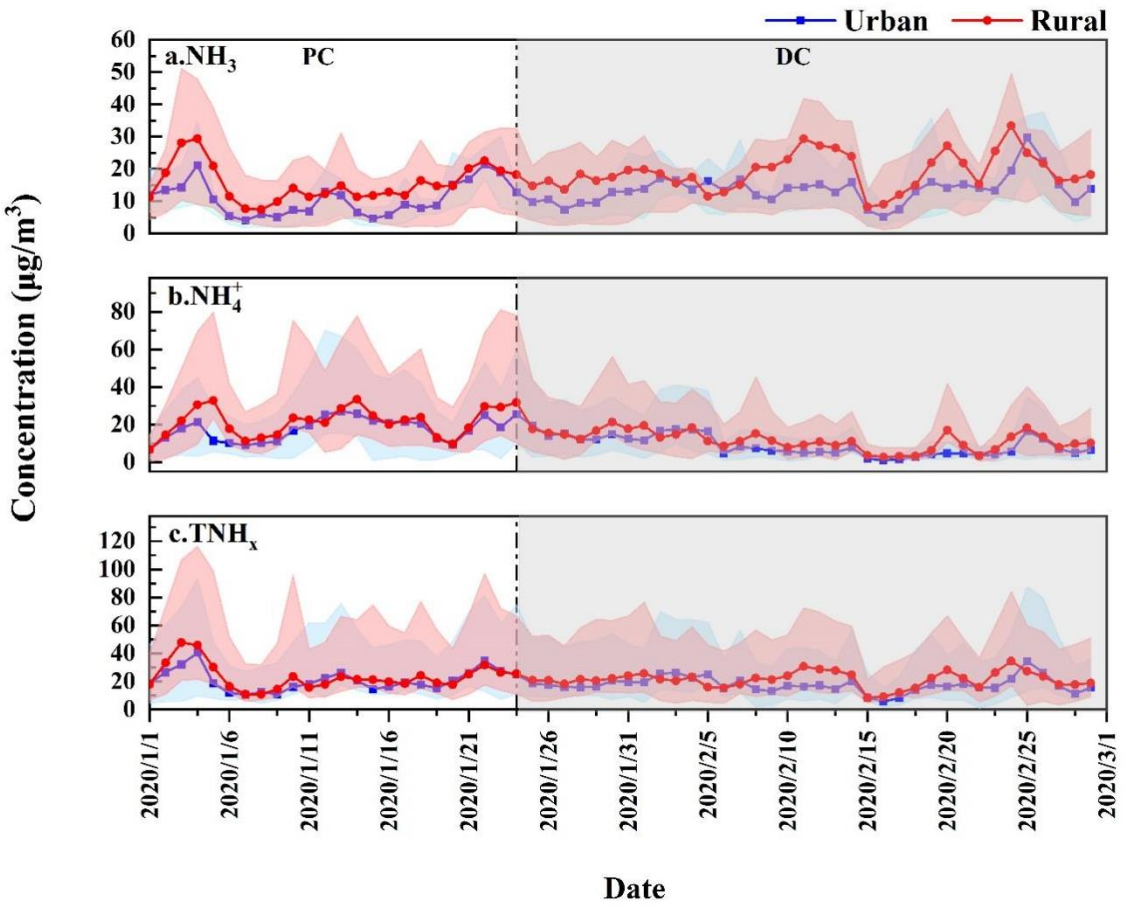

Figure 1. Temporal variations of a. NH_3, b. NH_4^+, and c. TNH_x at the urban and rural sites before (PC) and during (DC) the COVID-19 outbreak, respectively. The shaded areas of the curve represent the maximum and minimum values.

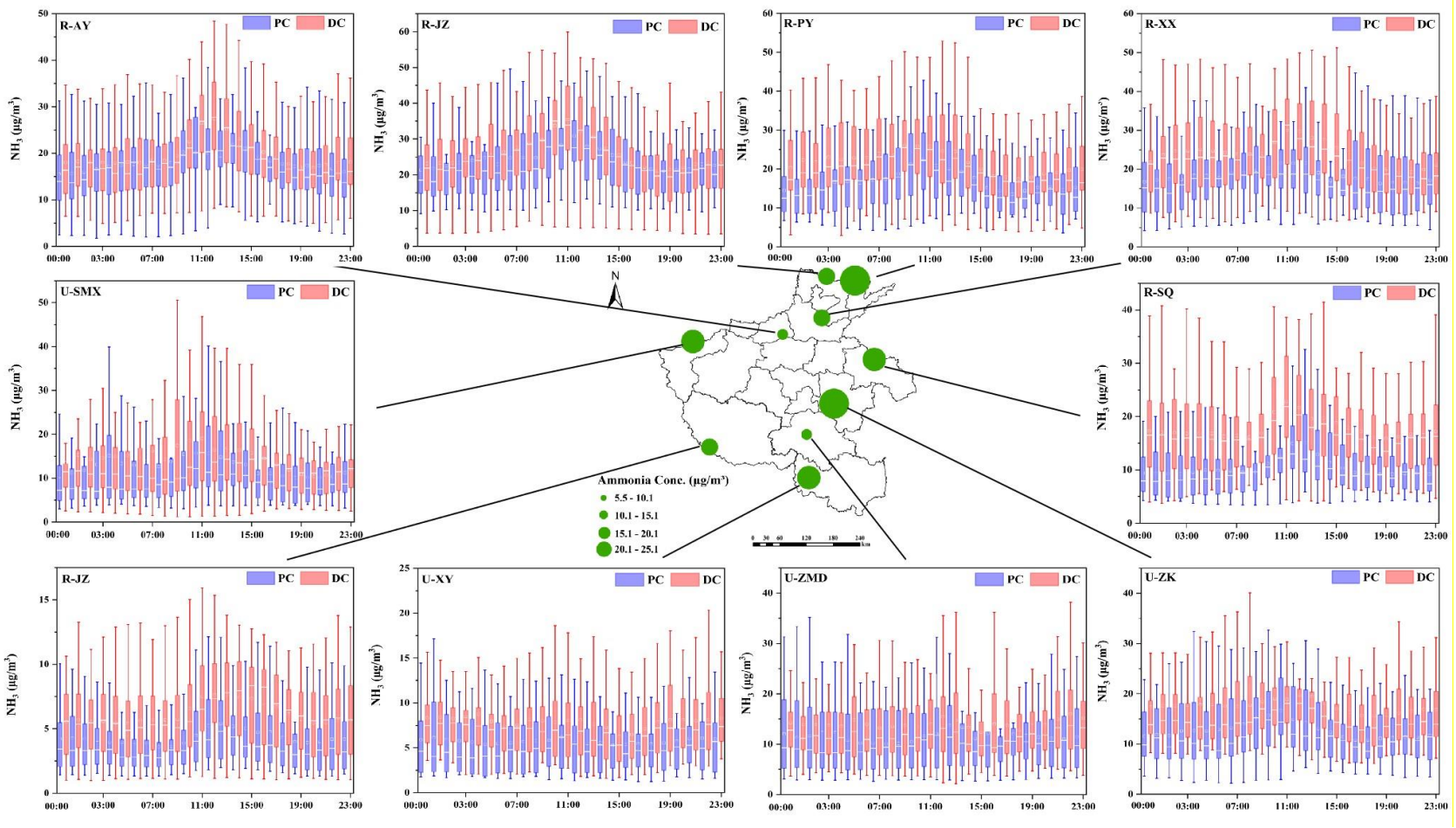

Figure 2. Daily variation of NH_3 concentrations at ten sites before (PC) and during (DC) the COVID-19 outbreak. The green dots represent the location of ten sites and their size represents the concentration of NH_3; In each box, the top, middle, and bottom lines represent the 75, 50, and 25 percentiles of statistical data, respectively; the upper and lower whiskers represent the 90 and 10 percentiles of statistical data, respectively.

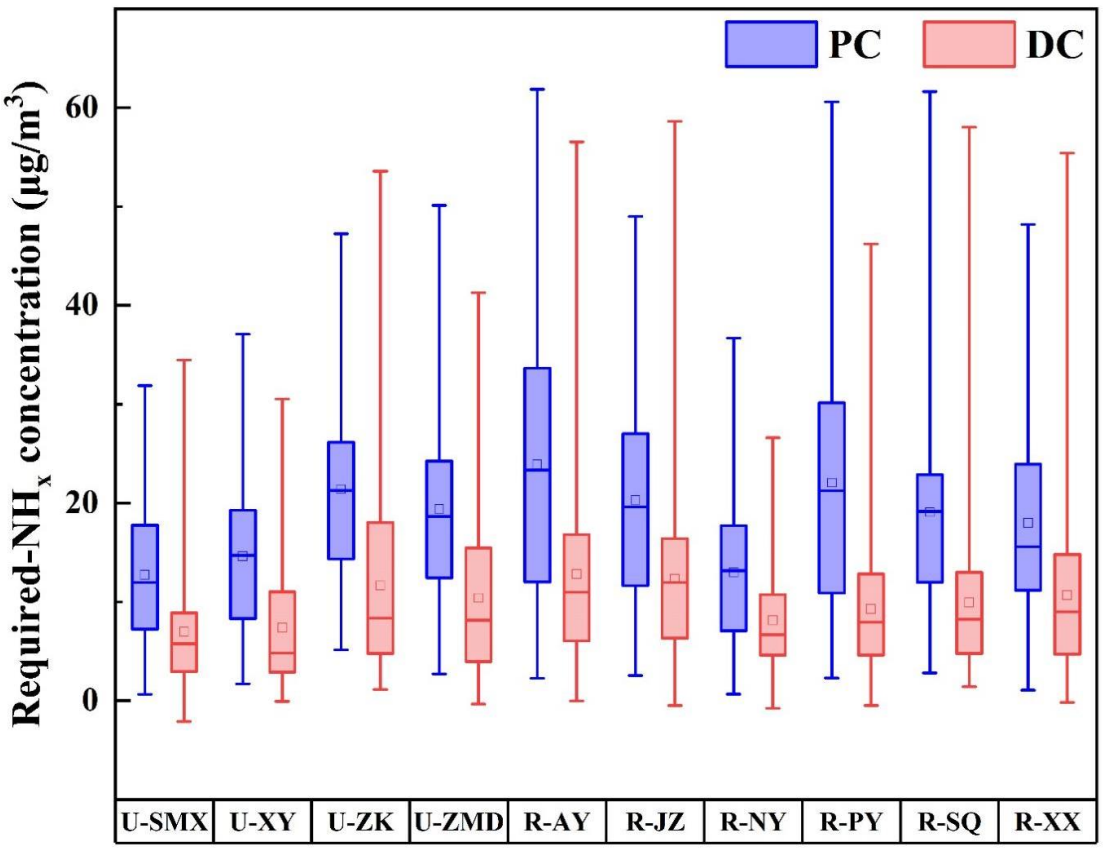

665

666 Figure 3. Box diagram of changes in Required-NH_x at ten sites before (PC) and during

667 (DC) the COVID-19 outbreak. In each box, the top, middle, and bottom lines represent

668 the 75, 50, and 25 percentiles of statistical data, respectively; the upper and lower

669 whiskers represent the 90 and 10 percentiles of statistical data, respectively.

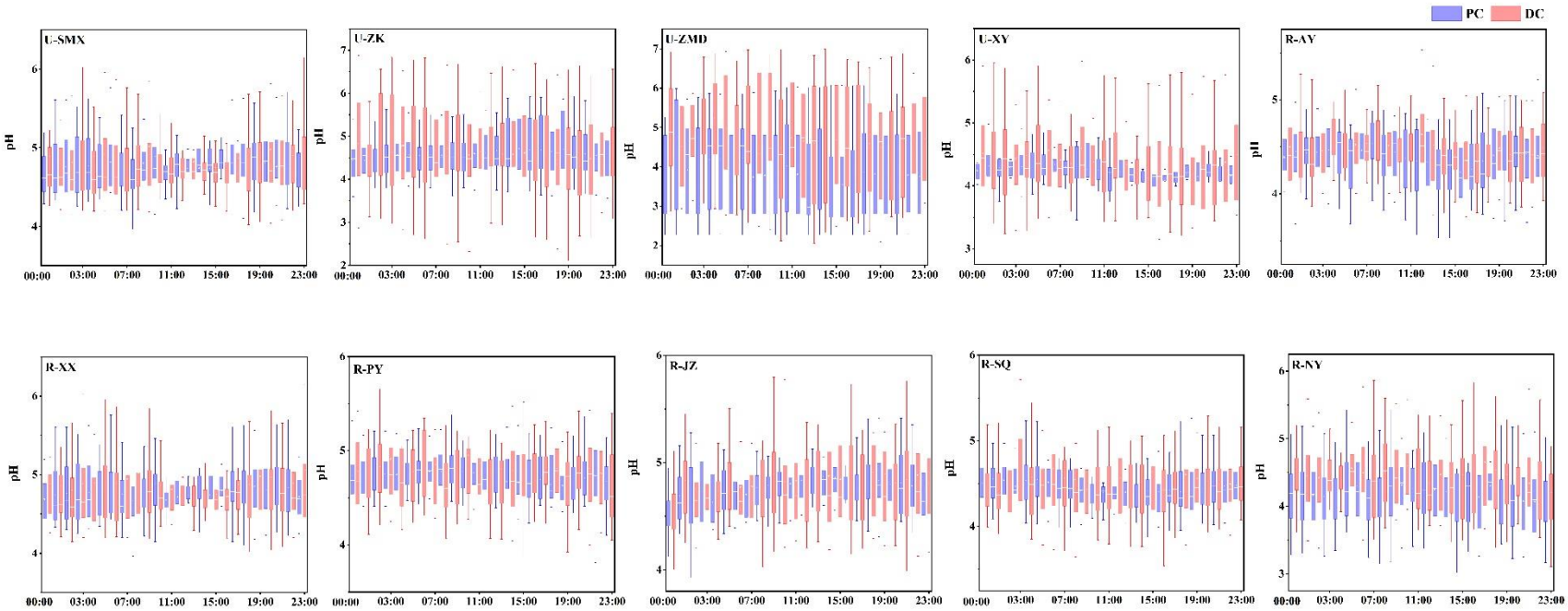

Figure 4. Diurnal patterns of pH at ten sites before (PC) and during (DC) the COVID-19 outbreak. In each box, the top, middle, and bottom lines represent the 75, 50, and 25 percentiles of statistical data, respectively; the upper and lower whiskers represent the 90 and 10 percentiles of statistical data, respectively.

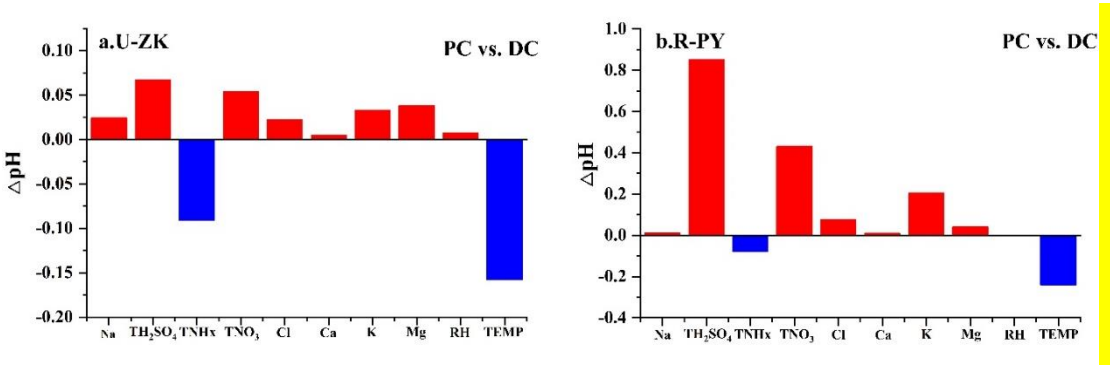

674

675 Figure 5. Changes of pH (ΔpH) through the sensitivity tests (Figure S5 and S6) by

676 changing parameters between PC and DC at the a. U-ZK and b. R-PY sites.

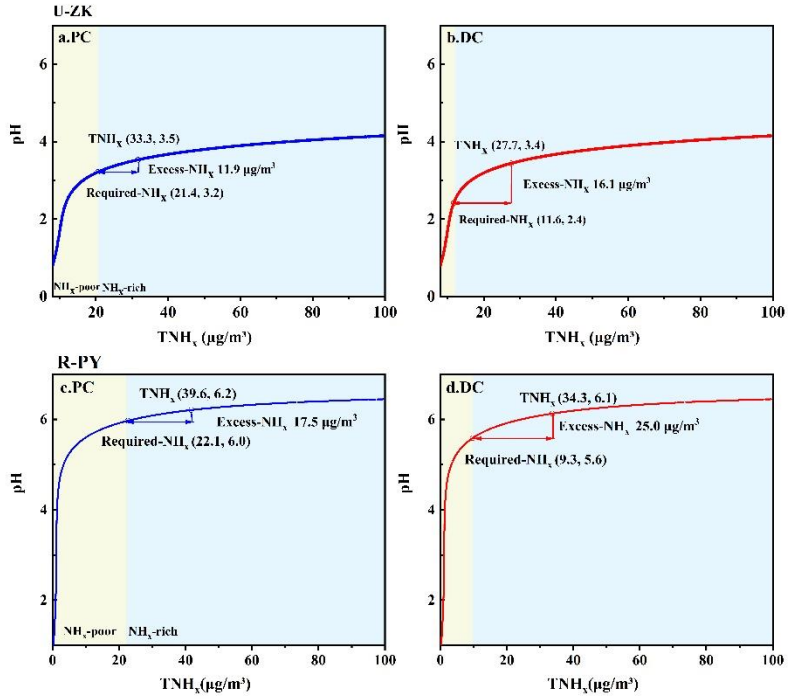

677

678 Figure 6. Particle pH corresponds to increasing TNH_x at U-ZK and R-PY sites to

679 examine the effects of major indicators of NH_3 (i.e., TNH_x, Required-NH_x, and Excess-

680 NH_x) on aerosol acidity. Particle pH was calculated by using a wide range of TNH_x

681 (25–130 μg/m^3) and average values of other parameters in PC and DC of U-ZK and R-

682 PY sites. The concentrations of TNH_x, Required-NH_x, and Excess-NH_x with

683 corresponding pH values are marked by a hollow box, hollow circle, and arrow

684 respectively. The yellow and blue background colors correspond to the NH_x-poor and

685 NH_x-rich, respectively.

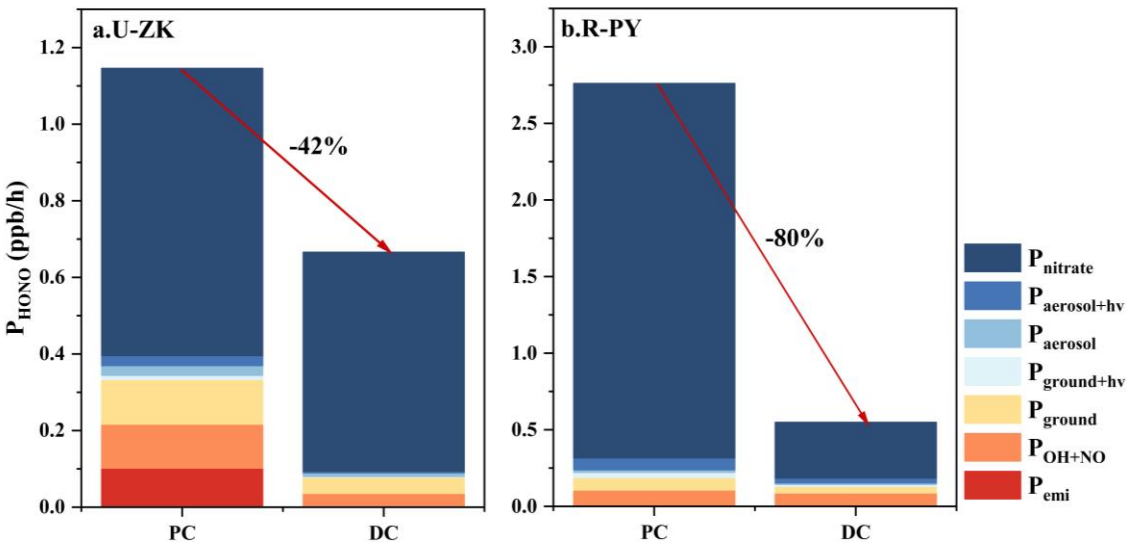

686

687 Figure 7. Comparison of HONO sources at a. U-ZK and b. R-PY sites before (PC) and

688 during (DC) the COVID-19 outbreak. The calculation method can be found in Text S4.

689

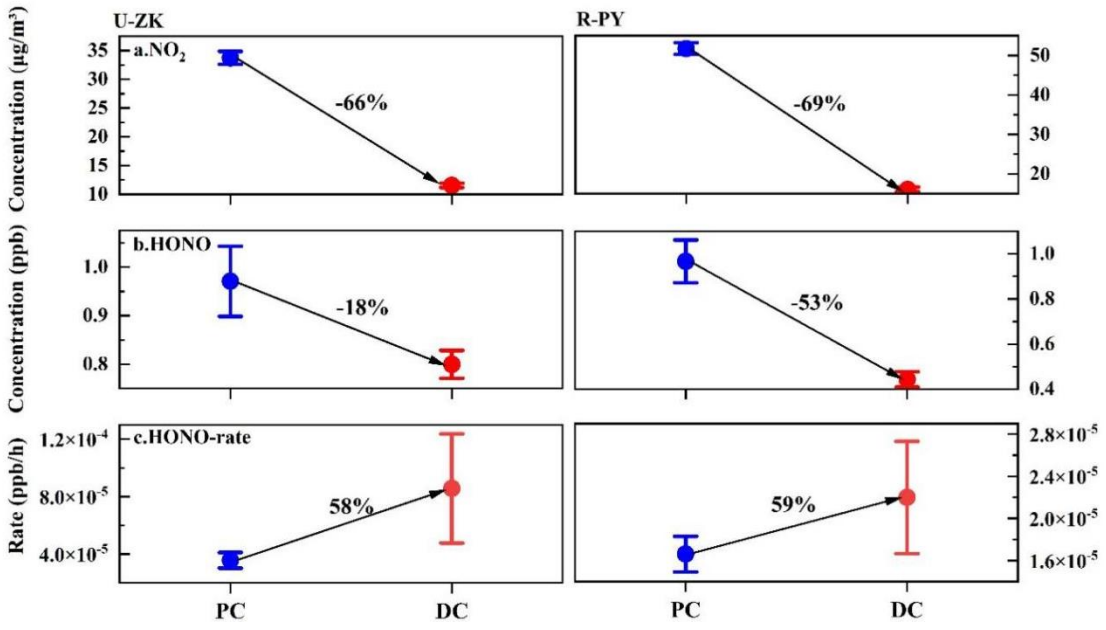

690

691 Figure 8. Decline ratios of a. NO_2, b. HONO concentration, and c. HONO production

692 rate at U-ZK and R-PY sites before (PC) and during (DC) the COVID-19 outbreak. The

693 center point represents the mean value, and the upper and lower whiskers represent the

694 95% confidence interval of the mean.

Table:

Table 1. Changes in concentrations (mean ± standard deviation) of NH_3, NH_4^+, and TNH_x at ten sites during entire periods (Average), before (PC), and during (DC) the COVID-19 outbreak.

Sites	Substances	Average (μg/m³)	PC (μg/m³)	DC (μg/m³)
U-SMX	NH_3	13.8 ± 10.8	12.6 ± 10.1	14.5 ± 11.1
	NH_4^+	10.9 ± 7.2	14.2 ± 7.2	8.8 ± 6.5
	TNH_x	22.9 ± 14.1	24.9 ± 14.5	21.7 ± 13.8
U-ZK	NH_3	15.6 ± 8.3	12.7 ± 6.5	17.4 ± 8.8
	NH_4^+	13.6 ± 9.3	19.1 ± 8.4	10.3 ± 8.1
	TNH_x	28.6 ± 13.7	30.9 ± 12.8	27.1 ± 14.0
U-ZMD	NH_3	13.1 ± 8.4	11.6 ± 8.2	14.0 ± 8.4
	NH_4^+	13.9 ± 9.8	19.6 ± 10.3	10.3 ± 7.5
	TNH_x	25.7 ± 14.6	30.3 ± 15.1	22.8 ± 13.5
U-XY	NH_3	7.0 ± 4.3	5.7 ± 4.0	7.9 ± 4.3
	NH_4^+	11.0 ± 7.7	15.4 ± 7.6	8.3 ± 6.5
	TNH_x	17.6 ± 9.8	20.6 ± 10.1	15.7 ± 9.2
R-AY	NH_3	19.0 ± 8.4	17.9 ± 8.3	19.7 ± 8.4
	NH_4^+	19.3 ± 12.9	26.4 ± 13.7	15.0 ± 10.3
	TNH_x	36.6 ± 18.2	41.7 ± 20.4	33.4 ± 16.0
R-XX	NH_3	21.7 ± 10.2	18.1 ± 9.3	23.8 ± 10.1
	NH_4^+	15.9 ± 10.4	20.6 ± 11.0	13.0 ± 8.8
	TNH_x	34.9 ± 17.0	35.1 ± 18.8	34.8 ± 15.8
R-PY	NH_3	19.8 ± 9.4	16.8 ± 8.1	21.7 ± 9.6
	NH_4^+	17.4 ± 11.8	25.3 ± 12.6	12.4 ± 8.0
	TNH_x	35.2 ± 17.8	39.4 ± 19.8	32.6 ± 15.7
R-JZ	NH_3	25.3 ± 11.5	24.1 ± 11.5	25.9 ± 11.4
	NH_4^+	17.3 ± 11.3	22.7 ± 11.6	14.2 ± 9.9
	TNH_x	40.8 ± 20.1	42.9 ± 22.8	33.5 ± 18.2
R-SQ	NH_3	15.0 ± 7.9	10.3 ± 5.2	17.7 ± 7.9
	NH_4^+	13.4 ± 8.5	18.9 ± 8.6	10.3 ± 6.7
	TNH_x	26.3 ± 13.2	25.5 ± 14.0	26.8 ± 12.7
R-NY	NH_3	5.5 ± 3.1	4.3 ± 2.7	6.2 ± 3.2
	NH_4^+	10.2 ± 6.9	13.3 ± 7.2	8.4 ± 6.1
	TNH_x	14.8 ± 8.5	16.0 ± 9.5	14.1 ± 7.8

Supplement materials:

Text S1 Detailed description of the aerosol and gas monitor.

The aerosol and gas monitor (MARGA, Metrohm, Switzerland) was used to analyze the hourly water-soluble ions (Na^+, NH_4^+, K^+, Mg^{2+}, Ca^{2+}, Cl^-, NO_3^-, and SO_4^{2-}) in $PM_{2.5}$, as well as gaseous species (NH_3, HNO_3, HCl, and HONO) at ten sampling sites. The atmospheric sample passes through a $PM_{2.5}$ cut-off head, and both particles and gases enter a wet rotating dissolution device for diffusion. Subsequently, the particles in the sample undergo hygroscopic growth and condensation in an aerosol supersaturated vapor generator, followed by collection and ion chromatographic analysis. The gases in the sample are oxidized by H_2O_2 in the dissolution device, absorbed into a liquid solvent, and then entered the gas sample collection chamber for ion chromatographic quantification. During this process, the sample is extracted through a liquid diffusion filter, where interfering acidic and alkaline gases are removed. To achieve high collection efficiency, the airflow containing loaded ions then enters an aerosol supersaturated collector until the particles can be injected into the ion chromatograph. The ion chromatography system utilizes either suppressor or non-suppressor conductivity detection methods for ion analysis. Before running the samples, the ion chromatograph system needs to be calibrated using standard solutions. By comparing the data obtained from the sample with the data obtained from known standard solutions, the identification and quantification of sample ions can be

performed. The data acquisition system generates chromatograms, and the chromatography software further converts each peak in the chromatogram into sample concentrations and outputs the results.

QA/QC

The instrument underwent daily checks and maintenance, which typically involved ensuring the stability of the internal standard response and maintaining a relative error within ±10% between the measured and theoretical concentrations of the internal standard. The system's data acquisition and transmission were carefully examined, along with monitoring the instrument's status information and collected data. This included checking parameters such as sampling flow rate, chromatographic column pressure, column temperature, conductivity, target compound peak retention time, and peak width to ensure their normal functioning. Regular replacement of consumables used by the instrument was carried out at predetermined intervals and frequencies. Additionally, standard curve measurements and calibration were performed in each season to guarantee the accuracy of the instrument's data. Calibration curve verification was performed at least once per quarter. A standard series containing at least 6 calibration points, including zero concentration, was prepared using standard solutions. The concentration range of the calibration curve was set according to the actual environmental concentration levels and determined by manual injection. The obtained calibration curve had a linear correlation coefficient (r) of ≥0.995. If this requirement was not met, the rationality of the internal standard solution concentration settings

would be checked. When key components such as the quantitative loop, chromatographic column, or suppressor are replaced, a new calibration curve will be promptly established. After establishing the new calibration curve, the sample sequence in the analysis software would be updated. The minimum detection limit was determined as follows: 0.002 μg/m^3 (Cl^-), 0.081 μg/m^3 (NH_4^+), 0.02 μg/m^3 (NO_3^-), 0.06 μg/m^3 (SO_4^{2-}), 0.002 μg/m^3 (Na^+), 0.08 μg/m^3 (K^+), 0.06 μg/m^3 (Ca^{2+}) and 0.007 μg/m^3 (Mg^{2+}). According to the research about the uncertainties in MARGA measurements, such as a 20% uncertainty for MARGA measurements (Song et al., 2018), an error of 10% for detecting SO_4^{2-}, NO_3^-, and HNO_3, and 15% for NH_3 and NH_4^+ (Rumsey et al., 2014), we set the uncertainties of 20% for NH_3 and NH_4^+, 10% for other components. Due to the complex conditions encountered during the actual sampling process, including variations in calibration slopes, sampling volumes, solvent concentrations, temperature, atmospheric pressure, and sampling flow rates at different sampling points, the assumed values mentioned above may not accurately reflect the actual situation.

Text S2 HONO measurement

The HONO monitoring method adopted in MARGA is the wet-flow diffusion tube method (WEDD) in the diffusion tube method (Zellweger, 1999; Takeuchi et al, 2013), which is a common method for measuring HONO in wet chemistry and has high absorption efficiency. The device adopts a vertical setting, through the diffusion tube, the air in the atmosphere is pulled upward from the bottom, and the absorbent liquid is transported to the top of the diffusion tube through the air pump. When flowing under the action of gravity, a thin absorbent liquid film will be generated on the inner surface of the tube by the tension. The absorbent liquid film will absorb HONO, and the solution at the bottom of the diffusion tube will be sucked out through the air pump. Then it is sent to the ion chromatography for analysis. The integration time of the sample mainly depends on the running time of the ion chromatography, which is about 5-30 min (Zellweger, 1999; Takeuchi et al, 2013). Based on the original, some scholars developed the flow injection-chemiluminescence method and used it together with WEDD for the measurement of HONO. The detection limit is about 0.03 $\mu g/m^3$ (Mikuska et al., 2008; Zhao et al., 2010). In addition, HONO observations measured with this AIM-IC system agree well with HONO observations measured with the other systems (VandenBoer et al., 2014). Therefore, it is feasible to measure HONO using this instrument.

Text S3 Detailed description of the NO_2、SO_2 and carbon analyzer.

The NO_2 analyzer utilized the chemiluminescence technique to measure the concentration of NO_2 in the air. This involved converting NO_2 to NO using a molybdenum converter, and then quantifying the NO concentration. The principle behind the SO_2 analyzer involved measuring the amount of ultraviolet light emitted during the decay of high-energy state SO_2. This emitted light was used to calculate the concentration of SO_2.

The carbon analyzer principle is primarily based on the NIOSH-5040 method, which involves analyzing the thermal optical transmittance of quartz filter samples. It employs a calibrated non-dispersive infrared sensor to detect the evolving carbon. Under controlled conditions with inert helium gas, carbon formed during a gradually increasing temperature gradient is referred to as OC, while carbon evolved under a mixture of 90% helium.

Text S4 Sources of HONO

4.1 Direct emission

HONO can be released directly into the atmosphere through vehicle exhaust (Burling et al., 2010; Veres et al., 2010). The lifetime of HONO in the atmosphere is relatively short, so vehicle emissions significantly contribute to urban atmospheric HONO (Chen et al., 2023; Liu et al., 2021a). Considering that there has been a

significant reduction in vehicle emissions in urban areas during DC. Additionally, the R-PY site is far from roads. Thus, vehicle emissions may not be the primary source of HONO for the U-ZK site during DC and R-PY sites during entire periods. To further validate the above conclusions, the conditional bivariate probability function diagrams of NO_2 at U-ZK and R-PY sites during PC and DC are depicted in Figure S2. NO_2 predominantly originated from long-distance transport at the U-ZK site during DC and the R-PY site during both PC and DC. Consequently, vehicle emissions are only calculated for the U-ZK site during the PC.

Here we use the $HONO/NO_x$ ratio to estimate HONO concentration, which is generally considered to be the vehicle emission factor (Kramer et al., 2020; Hao et al., 2020; Yu et al., 2022) for HONO. The calculation formula is as follows：

$$[HONO_{emi}] = 0.8\% \times [NO_x] \quad (1)$$

where $[HONO_{emi}]$ and $[NO_x]$ represent the HONO concentration emitted by vehicles and the observed NO_x concentration, respectively. Regarding previous studies (Table S3), 0.8% was selected as the vehicle emission factor, considering differences in vehicle type, fuel composition, and other factors (Kramer et al., 2020; Hao et al., 2020; Huang et al., 2017).

4.2 Homogeneous reaction of NO and •OH

The reaction between NO and •OH is the primary gas-phase reaction source of HONO at high NO concentrations, and the production rate contribution (P_{OH+NO}) for this

reaction can be calculated as:

$$P_{OH+NO} = k_{OH+NO}[OH][NO] \quad (2)$$

where k_{OH+NO} (7.2×10^{-12} cm^3 $molecule^{-1}$ s^{-1}) is the rate constant for the reactions at 298K (Li et al., 2012). •OH concentration was simulated according to the empirical model (Hu et al., 2022; Wang et al., 2025):

$$[OH] = 4.1\times10^{9} \times \frac{J(O^1D)\times J(NO_2)\times(140\times[NO_2]+1)+[HONO]\times J(HONO)}{0.41\times[NO_2]^2+1.7\times[NO_2]+1+[NO]\times k_{NO+OH}+[HONO]\times k_{NO+OH}} \quad (3)$$

where, J (O^1 D), J (NO_2), and J (HONO) are the photolysis rates calculated using the TUV model (v5.2; available at http://cprm.acom.ucar.edu/Models/TUV/). The cloud optical depth value for the TUV model was adjusted so that the predicted UVB radiation intensity matched the observations (Lyu et al., 2019; Wang et al., 2022b). The calculated •OH concentration varied from 0.1×10^6 to 4×10^6 molecule/cm^3 at U-ZK and 0.1×10^6 to 5×10^6 molecule/cm^3 t R-PY, which was comparable to the levels in other cities of North China (Li et al., 2018; Fuchs et al., 2017; Yang et al., 2017). Since there is no photolysis at night, the •OH concentration was assumed to be 0.8×10^6 molecule/cm^3 (Wang et al., 2022).

4.3 Heterogeneous conversion of NO_2 to HONO

4.3.1 Heterogeneous dark reactions

The heterogeneous conversion of NO_2 to HONO on the ground (P_{ground}) and on the aerosol surface ($P_{aerosol}$) was calculated based on parameters obtained from experiments or observations.

$$P_{ground} = \frac{1}{8}\gamma_1 \times [NO_2] \times C_{NO_2} \times \frac{S_g}{V} \quad (4)$$

$$P_{aerosol} = \frac{1}{4}\gamma_2 \times [NO_2] \times C_{NO_2} \times \frac{S_a}{V} \quad (5)$$

$$\frac{S_g}{V} = \frac{1}{MLH} \quad (6)$$

$$C_{NO_2} = \sqrt{\frac{8RT}{\pi M}} \quad (7)$$

where C_{NO2} is the average molecular velocity of NO_2 molecule (m s^{-1}); R is the ideal gas constant; T is the temperature (K); M is the molecular weight of NO_2 (kg mol^{-1}); MLH is the height of the mixed layer, which is determined to be 50 m due to HONO formation on the ground level and its short lifetime (Liu et al., 2020b); S_a/V is the surface area to volume ratio of aerosol, estimated by Su et al. (Su et al., 2008).

4.3.2 Heterogeneous photo-enhanced reactions

The heterogeneous photo-enhanced reactions of NO_2 on the surface of the ground ($P_{ground+hv}$) and the surface of the aerosol ($P_{aerosol+hv}$) were calculated following (Zhang et al., 2020a):

$$P_{ground+hv} = \frac{1}{8} \times C_{NO_2} \times \frac{1}{MLH} \times \gamma_1 \times \frac{J_{NO_2}}{J_{NO_2,noon}} \times [NO_2] \quad (8)$$

$$P_{aerosol+hv} = \frac{1}{4} \times C_{NO_2} \times \frac{S_a}{V} \times \gamma_2 \times \frac{J_{NO_2}}{J_{NO_2,noon}} \times [NO_2] \quad (9)$$

where JNO_2 and $JNO_{2,noon}$ are the photolysis rate of NO_2 and the photolysis rate of NO_2 at noon during the day, respectively.

γ_1 and γ_2 are the absorption coefficient of NO_2 on the ground and aerosol surface,

respectively, which is assumed to be 4×10^{-6} (Yu et al., 2022; Zhang et al., 2021; Zhang et al., 2020a). Moreover, we discuss the uncertainties based on the recommended values of 2×10^{-6}–1×10^{-5} as upper and lower bounds(Chen et al., 2023; VandenBoer et al., 2013; Wong et al., 2011). Results show (Figure S3) that the uncertainties for P_{ground}, $P_{aerosol}$, $P_{groung+hv}$, and $P_{aerosol+hv}$ are −50% to 150%, −50% to 151%, −20% to 120%, and −50% to 121% at the U-ZK, respectively. At the R-PY, the uncertainties for P_{ground}, $P_{aerosol}$, $P_{groung+hv}$, and $P_{aerosol+hv}$ are −50% to 150%, −50% to 151%, −20% to 120%, and −50% to 121%, respectively.

4.4 Nitrate photolysis

The nitrate photolysis ($P_{nitrate}$) was calculated based on the measured nitrate concentration (NO_3^-) from $PM_{2.5}$ and nitrate photolysis rate ($J_{nitrate \rightarrow HONO}$):

$$P_{nitrate} = J_{nitrate \rightarrow HONO} \times [NO_3^-] \quad (10)$$

where the $J_{nitrate \rightarrow HONO}$ was simulated by normalizing UV values, when the Zenit Angle is 0°, $J_{nitrate \rightarrow HONO}$ varied within the range of 1.22×10^{-5} to 4.84×10^{-4} s^{-1}, with an average value of 8.24×10^{-5} s^{-1} (Bao et al., 2018).

Text S5 Estimation of HONO formation rate

The redox reaction of NO_2 with SO_2 (R_1) is considered a crucial potential source of high concentrations of HONO in Northern China (Wang et al., 2016b; Cheng, 2016):

$$S(IV) + 2NO_2 + H_2O \rightarrow S(IV) + 2H^+ + 2NO_2^- \quad (R_1)$$

171 The rate expression for the reaction was estimated to:

172 $$d[S(VI)]/dt = k_1[NO_2][S(VI)], \quad (11)$$

173 where the $k_1 = (1.4\times10^5 + 1.24\times10^7)/2\ M^{-1}s^{-1}$ for the pH range < 5;

174 $k_1 = (23.25\times(pH–5) + 1.4 + 124)/2\times10^5\ M^{-1}s^{-1}$ for the pH range 5 < pH < 5.3;

175 $k_1 = (23.25\times(pH–5) + 1.4 + 12.6\times(pH–5.3) + 124)/2\times10^5\ M^{-1}s^{-1}$ for the pH range 5.3 <

176 pH < 5.8;

177 $k_1 = (12.6\times(pH–5.3) + 124+20)/2\times10^5\ M^{-1}s^{-1}$ for the pH range 5.8 < pH < 8.7;

178 and $k_1 = (2\times10^6 + 1.67\times10^7)/2\ M^{-1}s^{-1}$ for the pH range pH > 8.7. (Seinfeld et al., 1998)

179 In the above calculation formulas, the concentration of gas in the liquid is determined

180 by Henry's constant (H^*). The calculation formula is in Table S4. SO_2 has a dissociation

181 equilibrium in the solution, producing HSO_3^- and SO_3^{2-}. The ionization constants (K)

182 are shown in the following Table S5. The H* and K are temperature-dependent. The

183 values are given in Tables S4 and S5 under the condition of 298K, converted to the

184 value under the actual temperature using the following calculation formula:

185 $$H(T)\text{or } K(T) = H(T_{298K})\text{or}K(T_{298K})\exp\left[-\frac{\Delta H_{298K}}{R}\left(\frac{1}{T}-\frac{1}{298K}\right)\right] \quad (12)$$

186 where H(T)、K(T)、$H(T_{298K})$, and $K(T_{298K})$ represent the H* and K at actual temperature

187 and 298 K, respectively.

188 Influences of ionic strength on R_1 were not considered because of the high values

189 predicted by the ISORROPIA-II model during the sampling periods (Cheng et al.,

190 2016). To evaluate the effects of mass transport, the formulation of a standard resistance

191 model was adopted:

$$\frac{1}{R_{H,aq}} = \frac{1}{R_{aq}} + \frac{1}{J_{aq,lim}} \quad (13)$$

where $R_{H,aq}$ is the sulfate production rate, R_{aq} is the aqueous-phase reaction rate and $J_{aq,lim}$ is the limiting mass transfer rate. which could be calculated by the formulas as follows:

$$J_{aq,lim} = \min\{J_{aq}(SO_2), J_{aq}(X)\} \quad (14)$$

$$J_{aq}(X) = k_{MT}(X)\cdot[X] \quad (15)$$

where [X] refers to the aqueous-phase concentrations of SO_2 or the oxidants O_{xi} calculated by the equation in Table S4. The mass transfer rate coefficient $k_{MT}(X)$ (s^{-1}) can be calculated by:

$$k_{MT} = [\frac{R_p^2}{3D_g} + \frac{4R_p}{3\alpha v}]^{-1} \quad (16)$$

where R_p is the aerosol radius, D_g is the gas-phase molecular diffusion coefficient (0.2 $cm^2\ s^{-1}$ at 293K), v is the mean molecular speed of X (3×10^4 cm s^{-1}), and a is the mass accommodation of X on the droplet surface, and we adopted values of 0.11 and $2E^{-4}$ for SO_2 and NO_2, respectively referring to Cheng et al. (Cheng, 2016).

Figures

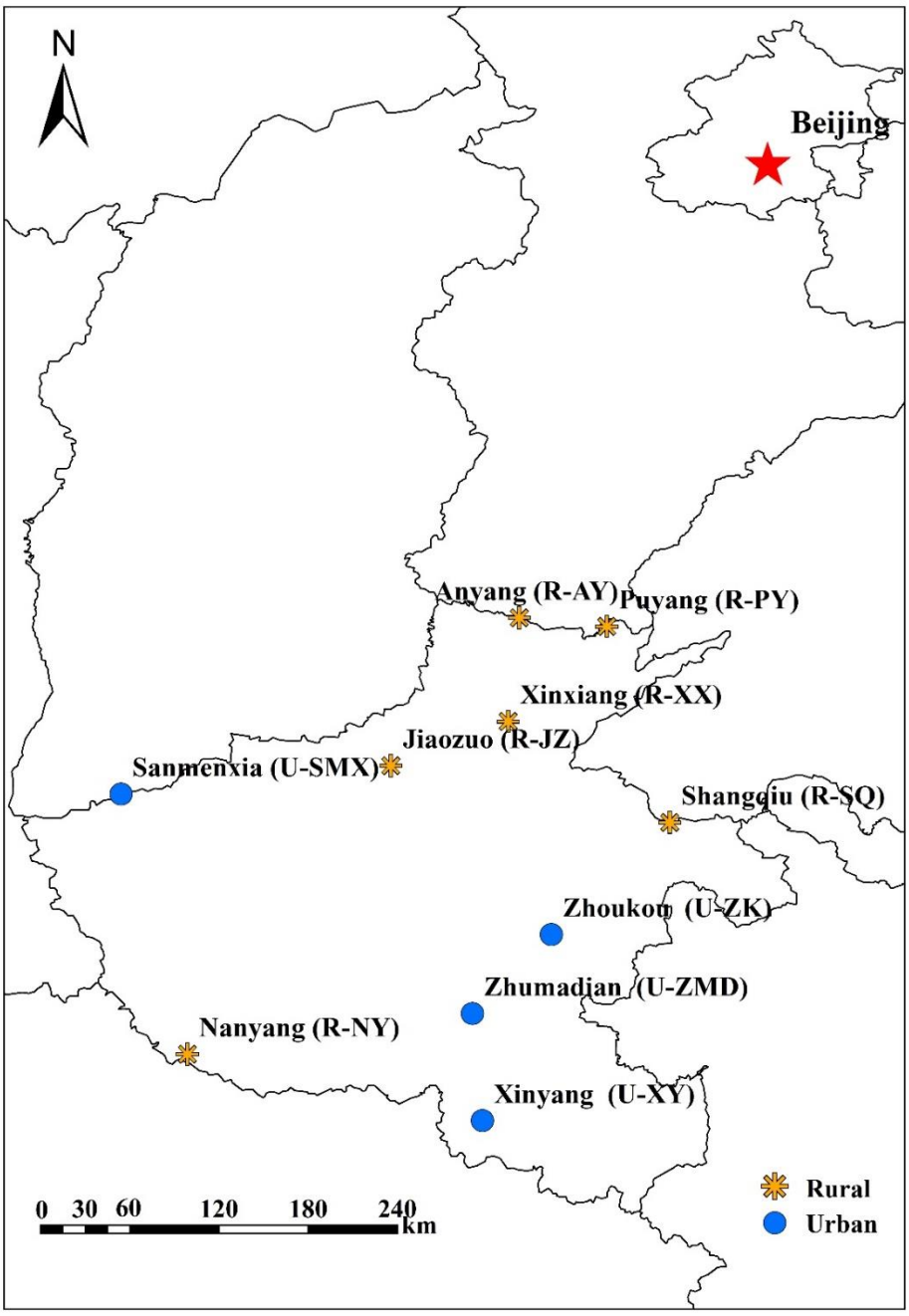

Figure S1. Sampling point map in Henan Province, China. © 2019 National Geomatics Center of China. i.e., urban sites at Sanmenxia (U-SMX), Zhoukou (U-ZK), Zhuamdian (U-ZMD) and Xinyang (U-XY), rural sites at Anyang (R-AY), Xinxiang (R-XX), Puyang (R-PY), Jiaozuo(R-JZ), Shangqiu (R-SQ) and Nanyang (R-NY). All rights reserved.

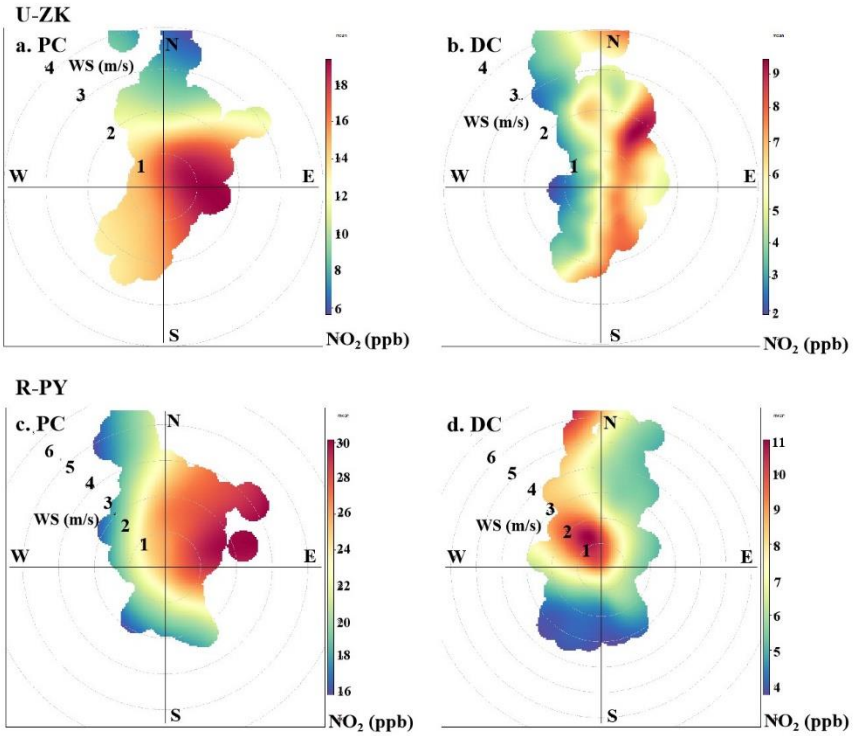

Figure S2. Result of conditional bivariate probability function plots: NO_2 at U-ZK and R-PY sites before (PC) and during (DC) the COVID-19 outbreak. The color scale bar represents NO_2 concentration.

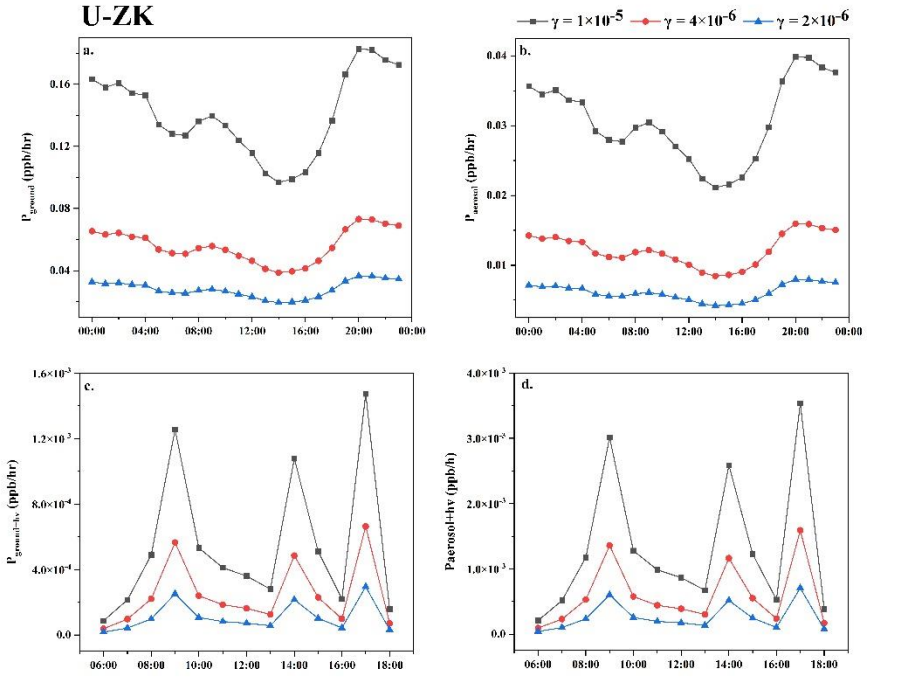

218

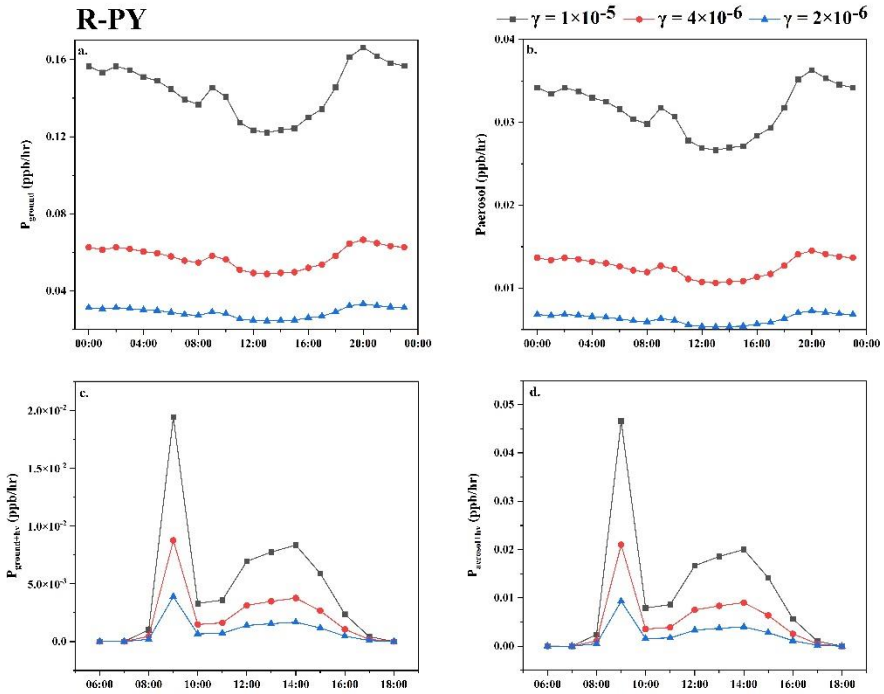

219

220 Figure S3. HONO production rate using different uptake rates of NO_2 at the U-ZK

221 and R-PY sites before (PC) and during (DC) the COVID-19 outbreak. (a)P_{ground}, (b)

222 $P_{aerosol}$, (c) $P_{ground+hv}$, and (d) $P_{aerosol+hv}$

223

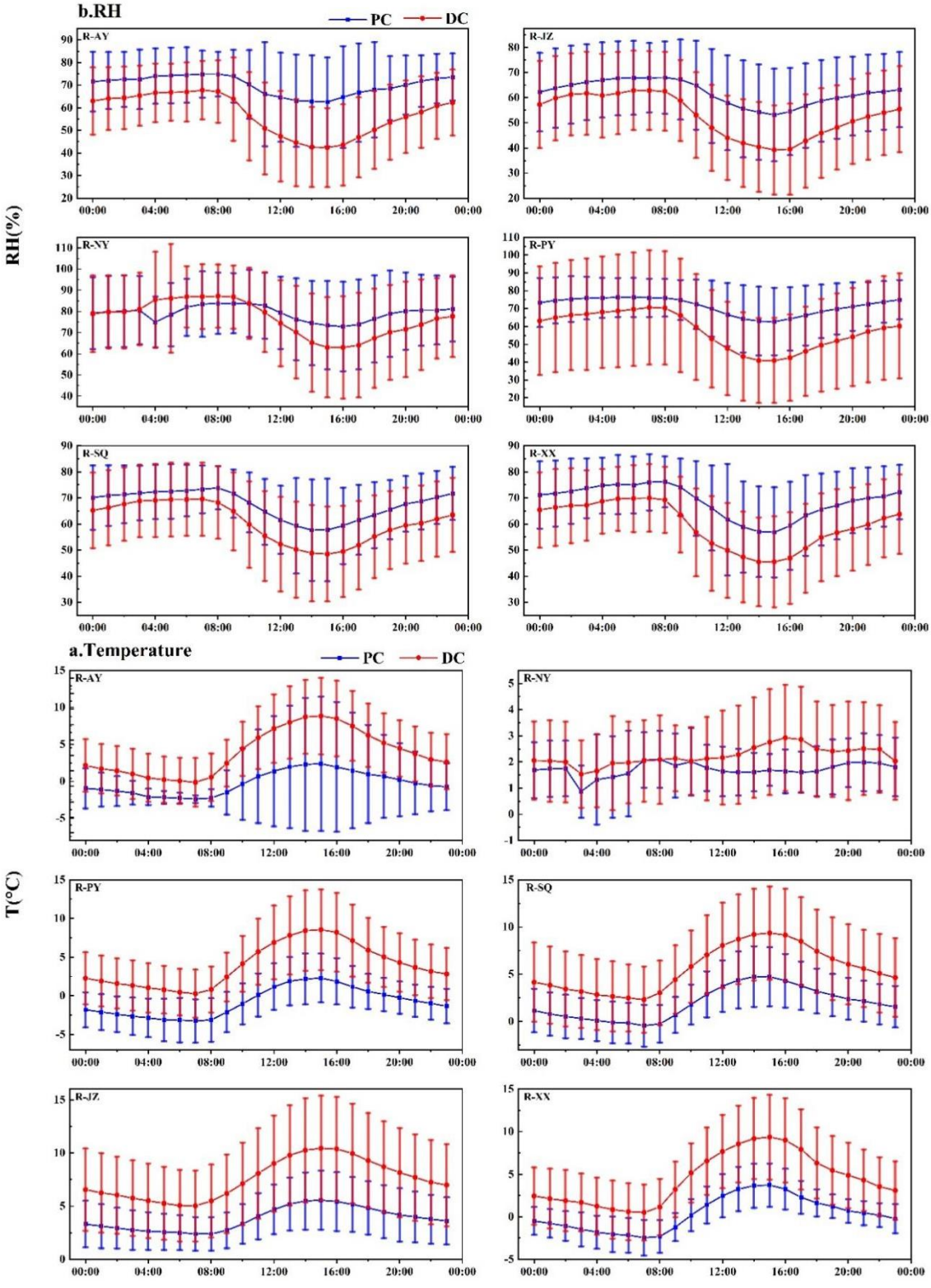

Figure S4. Daily changes in temperature and relative humidity (RH) in rural sites before (PC) and during (DC) the COVID-19 outbreak, the error bar represents the standard deviation. The upper and lower whiskers represent the standard deviation.

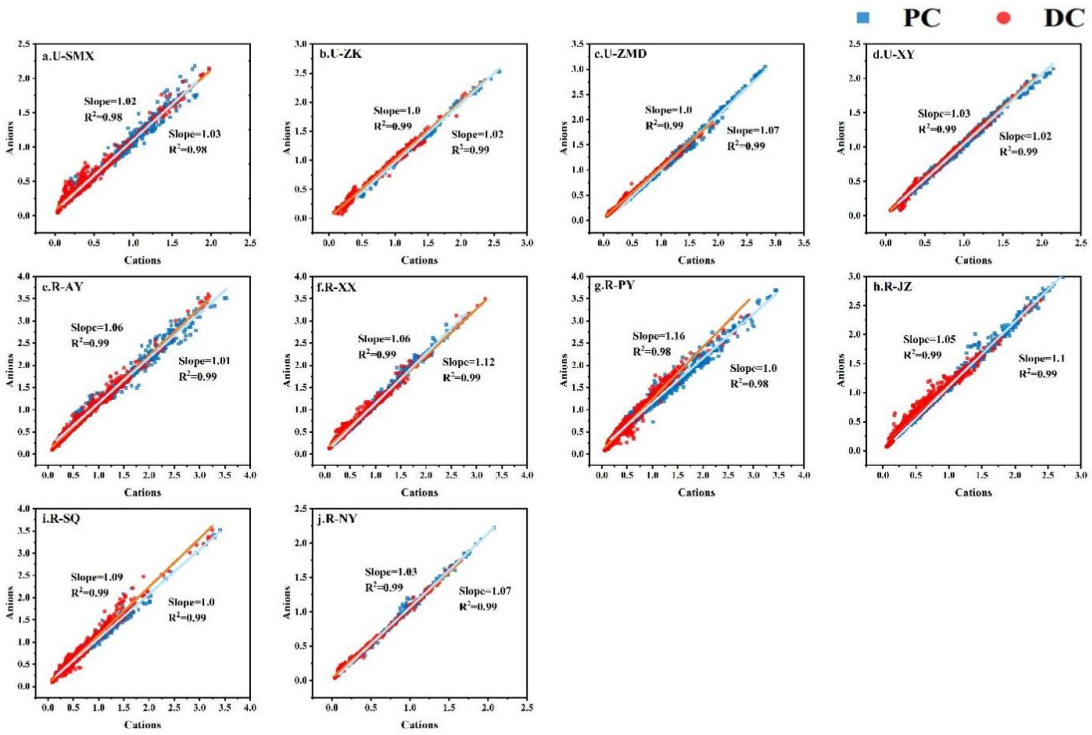

Figure S5. The equilibrium state of anions and cations at ten sites before (PC) and during (DC) the COVID-19 outbreak.

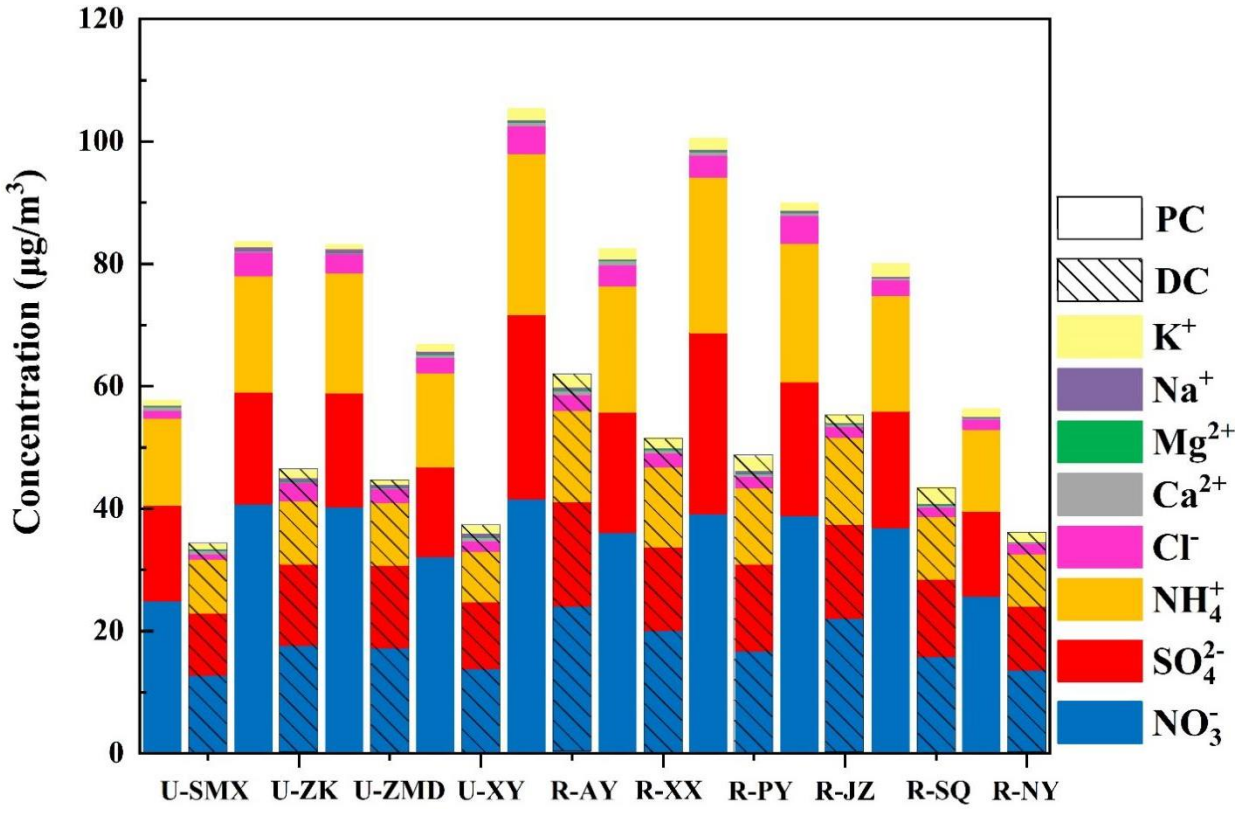

Figure S6. Concentrations of the water-soluble ions at the ten sites before (PC) and during (DC) the COVID-19 outbreak.

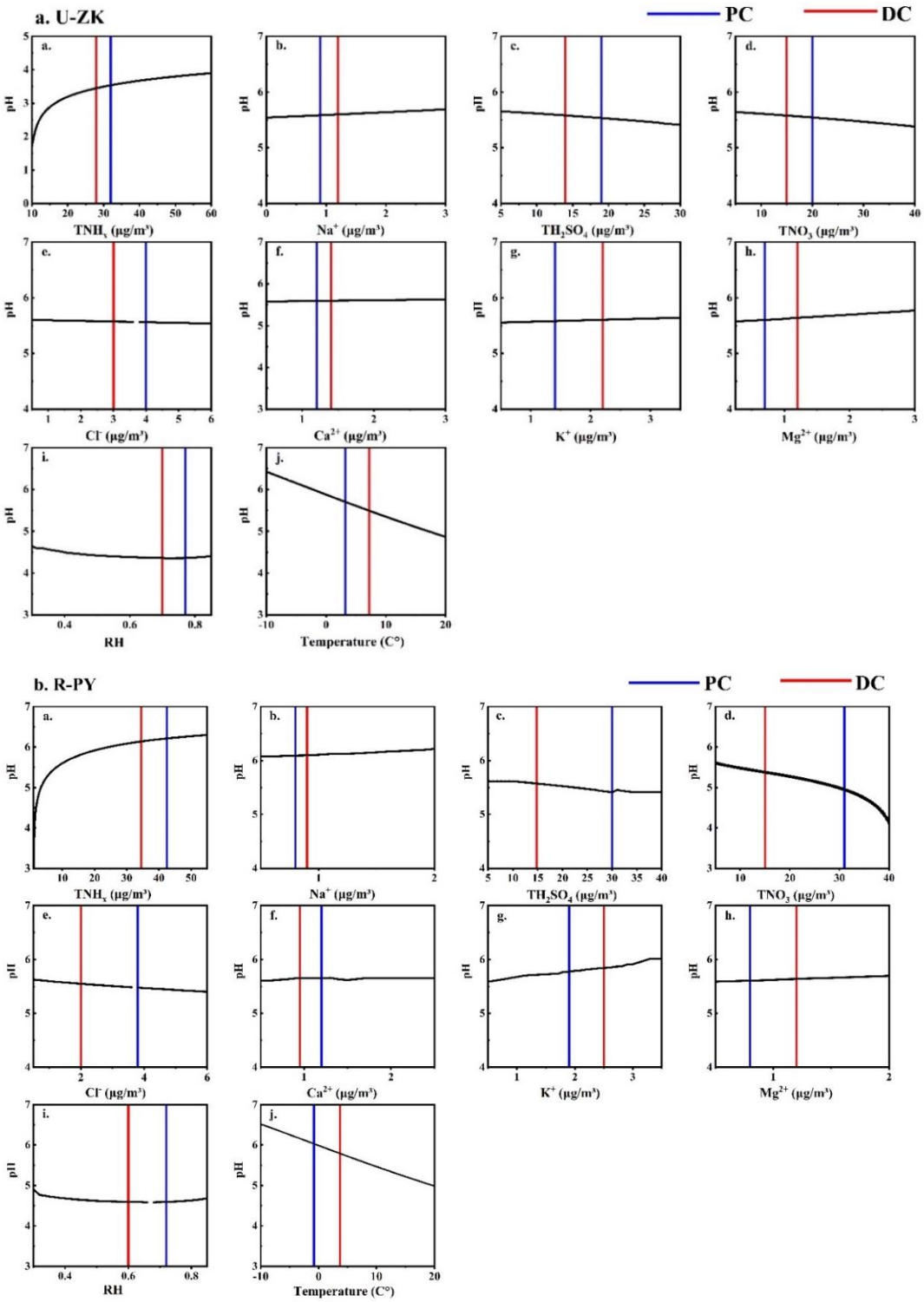

Figure S7. Sensitivity tests of pH to each factor. The vertical bar represents the mean values before (PC) and during (DC) the COVID-19 outbreak. A given range for a variable (i.e., TNH_x) with corresponding average values of other parameters (i.e., TH_2SO_4, TNO_3, TCl, TNa, K^+, Ca^{2+}, Mg^{2+}, T, and RH) was simulated to compare its effects on pH.

243

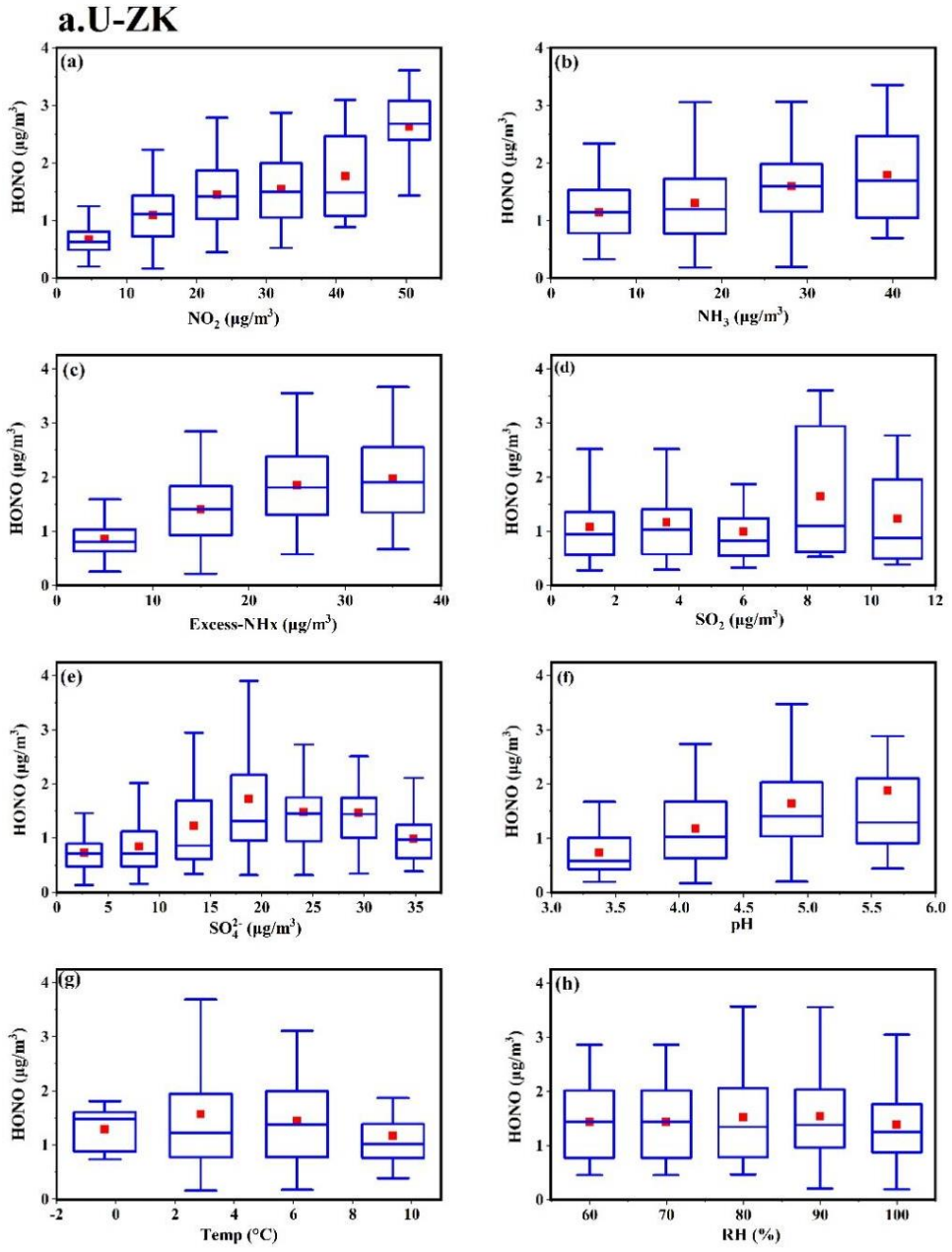
a.U-ZK
(a)
HONO (μg/m³)
NO₂ (μg/m³)
(b)
NH₃ (μg/m³)
(c)
Excess-NHx (μg/m³)
(d)
SO₂ (μg/m³)
(e)
SO₄²⁻ (μg/m³)
(f)
pH
(g)
Temp (°C)
(h)
RH (%)

244

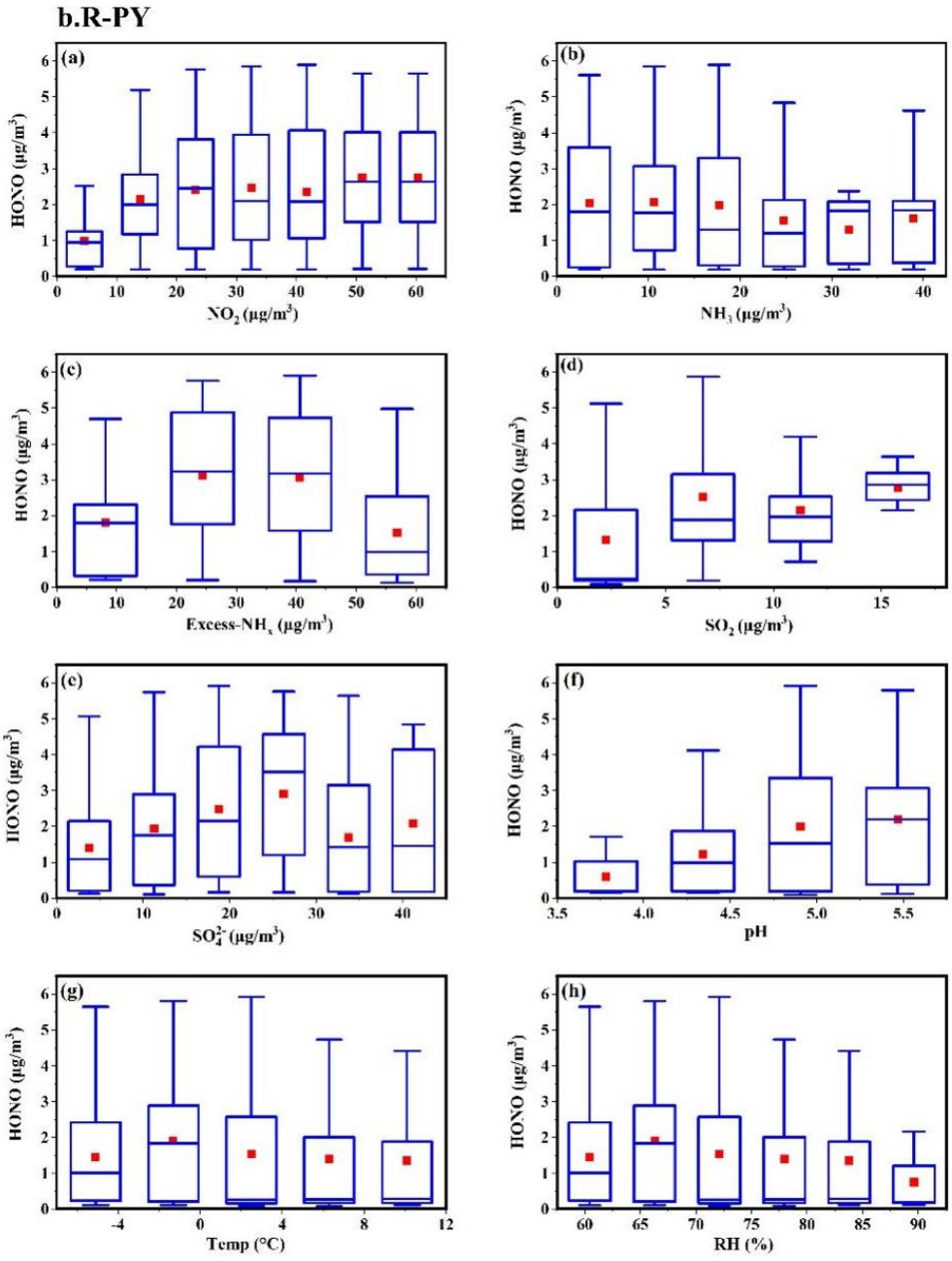

Figure S8. Relationship between HONO and main influencing factors during (DC) the COVID-19 outbreak at U-ZK and R-PY sites. In each box, the top, middle, and bottom lines represent the 75, 50, and 25 percentiles of statistical data, respectively; the upper and lower whiskers represent the 90 and 10 percentiles of statistical data, respectively.

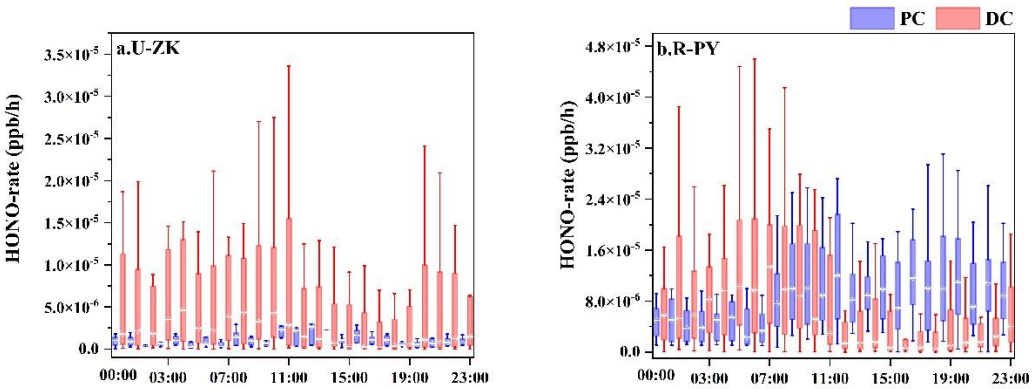

Figure. S9. HONO production rate through R_1 at U-ZK and R-PY sites before (PC) and during (DC) the COVID-19 outbreak. In each box, the top, middle, and bottom lines represent the 75, 50, and 25 percentiles of statistical data, respectively; the upper and lower whiskers represent the 90 and 10 percentiles of statistical data, respectively.

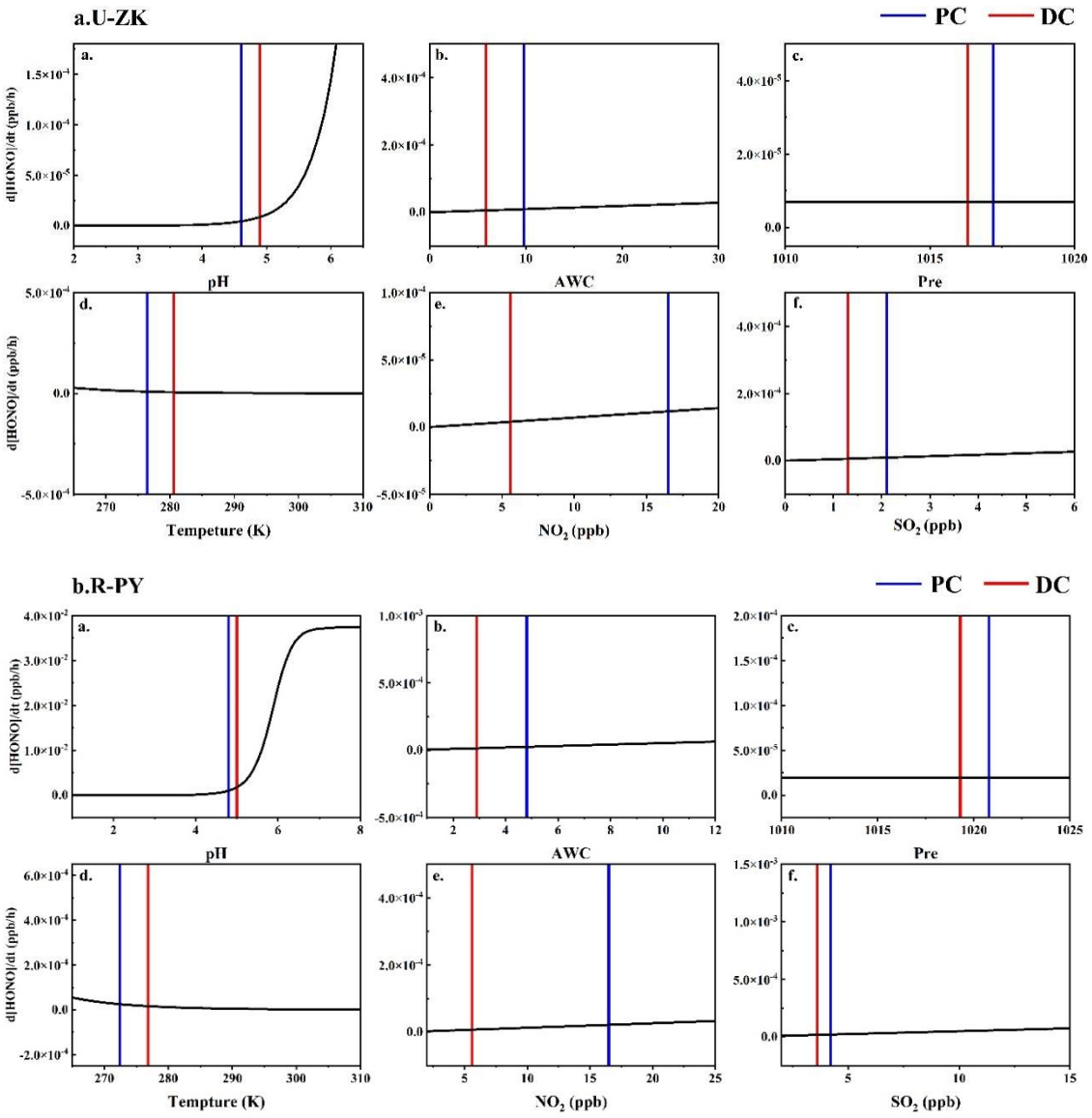

Figure S10. Sensitivity of HONO product rate to each factor. The vertical bar represents the mean values before (PC) and during (DC) the COVID-19 outbreak. The real-time measured values of a variable and the average values of other parameters were input into the production rate of the R_1 reaction.

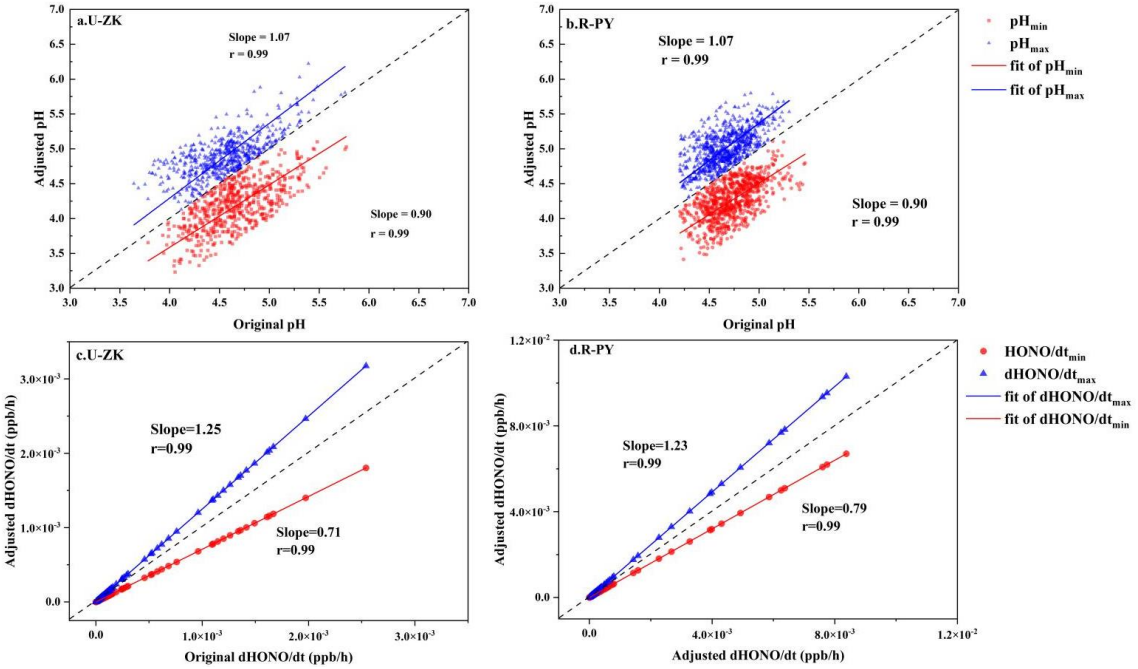

Figure S11. pH and R_1 uncertainties at the U-ZK and R-PY sites are based on two extreme scenarios of sensitivity to measurement uncertainty.

Tables

Table S1. Descriptions of the ten sampling sites in Henan Province, China.

Observation sites	Classifications	Abbreviations	Coordinates	Locations	Surrounding environment
Sanmenxia	Urban site	U-SMX	34.79 °N, 111.16 °E	Sanmenxia Environmental Protection Bureau	Roads, residential areas
Zhoukou	Urban site	U-ZK	33.65° N, 114.65° E	Chuanhui District People's Government	Roads, residential areas
Zhumadian	Urban site	U-ZMD	33.01° N, 114.01° E	Huanghuai College	Roads, residential areas, shopping malls
Xinyang	Urban site	U-XY	32.14° N, 114.09° E	Xinyang Museum	Roads, residential areas, shopping malls
Anyang	Rural site	R-AY	36.22°N, 114.39° E	Baizhuang Town Xindian North Street China Resources Gas (Andan Station)	Highways, villages, farmland
Xinxiang	Rural site	R-XX	35.38° N, 114.30° E	Banzao Township Central School in Yanjin County	Villages, farmland
Puyang	Rural site	R-PY	36.15° N, 115.10° E	Nanle County Longwang Temple Station	Villages, farmland
Jiaozuo	Rural site	R-JZ	35.02° N, 113.35° E	The Second River Bureau of Jiefeng Village, Beiguo Township, Wuxi County	Villages, farmland
Shangqiu	Rural site	R-SQ	34.56° N, 115.61° E	Liangyuan Huanghe Gudao National Forest Park	Highways, villages, farmland
Nanyang	Rural site	R-NY	32.68° N, 111.70° E	Nanyang Tangshan Park	Villages, farmland

Table S2. The value of ρ_s in other studies.

Observation site	Period	ρ_s (g/cm^3)	Reference
Beijing	Dec 2016	1.4	(Liu et al., 2017)
Tianjin	Dec-Jun 2015	1.3	(Shi et al., 2017)
Xi'an	Nov-Dec 2012	1.4	(Guo et al., 2017)
Hohhot	Winter 2015	1.35	(Wang et al., 2019)
Northeastern USA	Feb-Mar 2015	1.4	(Guo et al., 2016)
Crete, Greece	Aug-Nov 2012	1.35	(Bougiatioti et al., 2016)
Alabama, USA	Jun-Jul 2013	1.4	(Guo et al., 2015)
Georgia, USA	Aug-Oct 2016	1.4	(Nah et al., 2018)

Table S3. Summary of vehicle emission factors.

Observation site	Period	Emission factor (%)	Reference
Beijing	2020	0.79	(Meng et al., 2020)
Hong Kong	2015	0.4–1.8	(Yun et al., 2017)
Hong Kong	2011	0.5–1.6	(Xu et al., 2015)
Kiesberg Tunnel	2001	0.8	(Kleffmann et al., 2003)
Kiesberg Tunnel	1997	0.3–0.8	(Kurtenbach and Wiesen, 2001)
Guangzhou	2019	1.31	(Li et al., 2021b)

Table S4. Constants for calculating the apparent Henry's constant (H*).

Equilibrium	H (M atm^{-1}) at 298K	$-\triangle H_{298K}/R$ (K)
$SO_2(g) \leftrightarrow SO_2(aq)$	1.23	3145.3
$NO_2(g) \leftrightarrow NO_2(aq)$	1.00E-02	2516.2

Table S5. Constants for calculating the ionization constants (K).

Equilibrium	K (M) at 298K	$-\triangle H_{298K}/R$ (K)
$SO_2 \cdot H_2O \leftrightarrow H^+ + HSO_3^-$	1.30E-02	1960
$HSO_3^- \leftrightarrow H^+ + SO_3^{2-}$	6.60E-08	1500

281 Table S6. Comparisons of NH_3 concentrations (mean ± standard deviation) ($\mu g/m^3$)
282 from studies in other cities.

Sampling sites	Seasons	Years	NH_3 ($\mu g/m^3$)	Sites	References
Delhi, India	Winter	2013–2015	19.2 ± 3.5	Urban	(Saraswati et al., 2019)
Osaka, Japan	Winter	2015	1.5 ± 0.7	Urban	(Huy et al., 2017)
Toronto, Canada	Winter	2007	0.8 ± 0.5	Urban	(Hu et al., 2014)
Kanpur, India	Winter	2007	21.7 ± 5.8	Urban	(Behera and Sharma, 2010)
Nanjing	Winter	2014	6.7	Urban	(Wang et al., 2016b)
Yangtze River Delta	Winter	2019	9.3 ± 4.0	Urban	(Wang et al., 2021)
Shanghai	Winter	2014	2.8 ± 1.0	Urban	(Wang et al., 2018b)
Tianjin	Winter	2015	12.0	Urban	(Shi et al., 2019)
Xi'an	Winter	2012	17.5 ± 9.1	Urban	(Wang et al., 2016a)
Fujian	Winter	2016	12.8 ± 4.8	Urban	(Wu et al., 2017)
Beijing	Winter	2015	15.1 ± 2.9	Urban	(Wang et al., 2016a)
Beijing	Winter	2017	13.1 ± 1.6	Urban	(Zhang et al., 2020b)
Beijing	Winter	2020	19.9 ± 3.8	Urban	(Zhang et al., 2020b)
Taoyuan	Winter	2017–2018	1.7 ± 1.9	Urban	(Duan et al., 2021)
Zhengzhou	Winter	2018	19.0 ± 4.0	Rural	(Wang et al., 2020)
Quzhou	Winter	2019	29.5 ± 2.2	Rural	(Feng et al., 2022)
Gucheng	Winter	2016	9.3	Rural	(Xu et al., 2019)
Chongming	Winter	2019–2020	9.3 ± 4.0	Rural	(Lv et al., 2022)
Shanglan	Winter	2017–2018	2.5 ± 2.6	Rural	(Duan et al., 2021)

283

Table S7. The concentration (mean ± standard deviation) of relative humidity (RH), temperature (T), $\varepsilon(NH_4^+)$ at the ten sites before (PC) and during (DC) the COVID-19 outbreak.

Sites	Substances	Total	PC	DC
U-SMX	RH (%)	54.8 ± 18.0	60.6 ± 16.5	51.2 ± 18.0
	T (℃)	5.6 ± 4.2	3.1 ± 2.1	7.0 ± 4.4
	$\varepsilon(NH_4^+)$	0.43 ± 0.20	0.54 ± 0.18	0.36 ± 0.18
U-ZK	RH (%)	70.1 ± 21.9	73.6 ± 14.5	69.4 ± 22.4
	T (℃)	6.4 ± 4.3	3.8 ± 2.3	7.0 ± 4.5
	$\varepsilon(NH_4^+)$	0.43 ± 0.20	0.59 ± 0.14	0.32 ± 0.17
U-ZMD	RH (%)	74.9 ± 23.3	84.4 ± 17.8	68.9 ± 24.4
	T (℃)	5.6 ± 4.6	2.9 ± 2.7	7.4 ± 4.8
	$\varepsilon(NH_4^+)$	0.48 ± 0.21	0.62 ± 0.17	0.38 ± 0.18
U-XY	RH (%)	77.0 ± 22.1	86.7 ± 13.3	74.3 ± 23.3
	T (℃)	7.7 ± 4.5	4.7 ± 2.2	8.5 ± 4.6
	$\varepsilon(NH_4^+)$	0.55 ± 0.21	0.71 ± 0.14	0.45 ± 0.18
R-AY	RH (%)	62.2 ± 17.9	70.1 ± 14.9	57.2 ± 17.8
	T (℃)	2.6 ± 0.9	-0.2 ± 2.5	4.4 ± 4.7
	$\varepsilon(NH_4^+)$	0.46 ± 0.17	0.57 ± 0.15	0.39 ± 0.14
R-XX	RH (%)	63.0 ± 17.0	68.7 ± 14.6	59.5 ± 17.5
	T (℃)	2.9 ± 4.6	0.3 ± 2.8	4.4 ± 4.8
	$\varepsilon(NH_4^+)$	0.40 ± 0.17	0.52 ± 0.16	0.35 ± 0.14
R-PY	RH (%)	63.6 ± 18.0	71.5 ± 14.6	57.6 ± 18.0
	T (℃)	1.7 ± 4.8	-0.8 ± 3.2	3.6 ± 4.9
	$\varepsilon(NH_4^+)$	0.43 ± 0.17	0.58 ± 0.13	0.34 ± 0.13
R-JZ	RH (%)	56.3 ± 18.5	62.0 ± 16.7	52.8 ± 18.7
	T (℃)	4.1 ± 4.4	1.7 ± 2.6	5.6 ± 4.7
	$\varepsilon(NH_4^+)$	0.37 ± 0.14	0.46 ± 0.13	0.32 ± 0.13
R-SQ	RH (%)	63.2 ± 15.6	67.5 ± 12.6	60.5 ± 17.0
	T (℃)	4.2 ± 4.5	2.0 ± 2.9	5.6 ± 4.7
	$\varepsilon(NH_4^+)$	0.45 ± 0.19	0.63 ± 0.12	0.35 ± 0.14
R-NY	RH (%)	75.9 ± 19.1	79.3 ± 17.7	73.9 ± 19.6
	T (℃)	5.7 ± 3.8	3.6 ± 2.6	6.9 ± 3.9
	$\varepsilon(NH_4^+)$	0.59 ± 0.19	0.73 ± 0.12	0.52 ± 0.18

Table S8. The concentration (mean ± standard deviation) of required ammonia (Required-NH_x) and excess ammonia (Excess-NH_x) at the ten sites before (PC) and during (DC) the COVID-19 outbreak.

Sites	Substances	Total (μg/m³)	PC (μg/m³)	DC (μg/m³)
U-SMX	Required-NH_4^+	9.1 ± 7.1	12.7 ± 7.1	7.0 ± 6.2
	Excess-NH_4^+	14.7 ± 11.2	13.6 ± 10.4	15.3 ± 11.6
U-ZK	Required-NH_4^+	15.2 ± 9.6	21.4 ± 8.6	11.6 ± 8.4
	Excess-NH_4^+	14.6 ± 8.3	11.9 ± 6.0	16.1 ± 9.0
U-ZMD	Required-NH_4^+	13.9 ± 9.8	19.4 ± 9.8	10.4 ± 8.0
	Excess-NH_4^+	12.8 ± 8.7	11.6 ± 8.2	13.6 ± 8.8
U-XY	Required-NH_4^+	10.2 ± 7.5	14.6 ± 7.3	7.4 ± 6.2
	Excess-NH_4^+	7.8 ± 4.6	6.5 ± 4.4	8.7 ± 4.5
R-AY	Required-NH_4^+	17.1 ± 12.4	23.9 ± 13.4	12.8 ± 9.5
	Excess-NH_4^+	21.2 ± 9.4	20.2 ± 9.2	21.9 ± 9.4
R-XX	Required-NH_4^+	13.5 ± 9.6	18.0 ± 9.8	10.7 ± 8.2
	Excess-NH_4^+	23.3 ± 11.4	19.6 ± 10.8	25.6 ± 11.2
R-PY	Required-NH_4^+	13.8 ± 11.0	22.1 ± 12.5	9.3 ± 6.6
	Excess-NH_4^+	22.3 ± 10.8	17.5 ± 8.6	25.0 ± 11.0
R-JZ	Required-NH_4^+	15.4 ± 10.4	20.3 ± 10.6	12.5 ± 9.1
	Excess-NH_4^+	27.5 ± 12.9	26.0 ± 13.1	28.4 ± 12.7
R-SQ	Required-NH_4^+	13.2 ± 9.1	19.1 ± 8.9	9.9 ± 7.3
	Excess-NH_4^+	15.1 ± 8.6	10.1 ± 5.4	17.9 ± 8.7
R-NY	Required-NH_4^+	9.9 ± 6.6	13.0 ± 6.9	8.1 ± 5.8
	Excess-NH_4^+	6.0 ± 3.6	4.4 ± 3.3	6.9 ± 3.4

293 Table S9. Comparison of the particle pH values in this study (PC/DC) and other sites
294 (mean or mean ± standard).

	Sites	Periods	pH	References
Urban	Sanmenxia	Jan–Feb 2020	4.6 ± 0.5/4.8 ± 0.9	This study
	Zhoukou	Jan–Feb 2020	4.6 ± 0.6/5.1 ± 0.4	
	Zhumadian	Jan–Feb 2020	4.6 ± 0.3/4.8 ± 1.2	
	Xinyang	Jan–Feb 2020	4.2 ± 0.3/4.6 ± 1.3	
Rural	Anyang	Jan–Feb 2020	4.5 ± 0.4/4.6 ± 0.8	
	Xinxiang	Jan–Feb 2020	4.8 ± 0.5/4.9 ± 0.9	
	Puyang	Jan–Feb 2020	4.8 ± 0.3/5.1 ± 0.9	
	Jiaozuo	Jan–Feb 2020	4.9 ± 0.5/5.1 ± 0.8	
	Shangqiu	Jan–Feb 2020	4.5 ± 0.3/4.7 ± 0.8	
	Nanyang	Jan–Feb 2020	4.2 ± 0.5/4.4 ± 0.7	
Urban	Beijing	Jan–Feb 2015	4.5	(Guo et al., 2017)
	Beijing	Dec 2016	4.3 ± 0.4	(Liu et al., 2017)
	Beijing	Feb 2017	4.5 ± 0.7	(Ding et al., 2019)
	Tianjin	Dec–Jun 2015	4.9 ± 1.4	(Shi et al., 2017)
	Tianjin	Aug 2015	3.4 ± 0.5	(Shi et al., 2019)
	Hohhot	Winter	5.7	(Wang et al., 2019)
	Mt. Tai	Summer	2.9 ± 0.5	(Liu et al., 2021b)
	Taoyuan	Nov 2017–Jan 2018	5.1 ± 1.0	(Duan et al., 2021)
	Zhengzhou	Jan 2018	4.5	(Wang et al., 2020)
	Anyang	Jan 2018	4.8	(Wang et al., 2020)
Mountain	Mt. Tai	Summer	3.6 ± 0.7	(Liu et al., 2021b)
Rural	Shanglan	Nov 2017–Jan 2018	5.5 ± 1.1	(Duan et al., 2021)

295

References

Behera, S. N., and Sharma, M.: Investigating the potential role of ammonia in ion chemistry of fine particulate matter formation for an urban environment, Sci. Total Environ., 408, 3569–3575, https://doi.org/10.1016/j.scitotenv.2010.04.017, 2010.

Bougiatioti, A., Nikolaou, P., Stavroulas, I., Kouvarakis, G., Weber, R., Nenes, A., Kanakidou, M., and Mihalopoulos, N.: Particle water and pH in the eastern Mediterranean: source variability and implications for nutrient availability, Atmos. Chem. Phys., 16, 4579–4591, https://doi.org/10.5194/acp-16-4579-2016, 2016.

Burling, I. R., Yokelson, R. J., Griffith, D. W. T., Johnson, T. J., Veres, P., Roberts, J. M., Warneke, C., Urbanski, S. P., Reardon, J., Weise, D. R., Hao, W. M., and de Gouw, J.: Laboratory measurements of trace gas emissions from biomass burning of fuel types from the southeastern and southwestern United States, Atmos. Chem. Phys., 10, 11115–11130, https://doi.org/10.5194/acp-10-11115-2010, 2010.

Chen, D., Zhou, L., Liu, S., Lian, C., Wang, W., Liu, H., Li, C., Liu, Y., Luo, L., Xiao, K., Chen, Y., Qiu, Y., Tan, Q., Ge, M., and Yang, F.: Primary sources of HONO vary during the daytime: Insights based on a field campaign, Sci. Total Environ., 903, https://doi.org/10.1016/j.scitotenv.2023.166605, 2023.

Cheng, Y., Zheng, G., Wei, C., Mu, Q., Zheng, B., Wang, Z., Gao, M., Z., Q., He, K., Carmichael, G., Pöschl, U., and Su, and H.: Reactive nitrogen chemistry in aerosol water as a source of sulfate during haze events in China, Sci. Adv. 2, e1601530., https://doi.org/10.1126/sciadv.1601530, 2019.

Ding, J., Zhao, P., Su, J., Dong, Q., Du, X., and Zhang, Y.: Aerosol pH and its driving factors in Beijing, Atmos. Chem. Phys. 19, 7939–7954, https://doi.org/10.5194/acp-19-7939-2019, 2019.

Duan, X., Yan, Y., Peng, L., Xie, K., Hu, D., Li, R., and Wang, C.: Role of ammonia in

secondary inorganic aerosols formation at an ammonia-rich city in winter in North China: A comparative study among industry, urban, and rural sites, Environ. Pollut., 291, 118151, https://doi.org/10.1016/j.envpol.2021.118151, 2021.

Feng, S., Xu, W., Cheng, M., Ma, Y., Wu, L., Kang, J., Wang, K., Tang, A., Collett, J. L., Fang, Y., Goulding, K., Liu, X., and Zhang, F.: Overlooked nonagricultural and wintertime agricultural NH_3 emissions in Quzhou county, North China Plain: evidence from ^{15}N-Stable Isotopes. Environ. Sci. Technol. Lett. 9, 127–133, https://doi.org/10.1021/acs.estlett.1c00935, 2022.

Fuchs, H., Tan, Z., Lu, K., Bohn, B., Broch, S., Brown, S. S., Dong, H., Gomm, S., Häseler, R., He, L., Hofzumahaus, A., Holland, F., Li, X., Liu, Y., Lu, S., Min, K.-E., Rohrer, F., Shao, M., Wang, B., Wang, M., Wu, Y., Zeng, L., Zhang, Y., Wahner, A., and Zhang, Y.: OH reactivity at a rural site (Wangdu) in the North China Plain: contributions from OH reactants and experimental OH budget, Atmos. Chem. Phys., 17, 645–661, https://doi.org/10.5194/acp-17-645-2017, 2017.

Guo, H., Xu, L., Bougiatioti, A., Cerully, K. M., Capps, S. L., Hite, J. R., Carlton, A. G., Lee, S. H., Bergin, M. H., Ng, N. L., Nenes, A., and Weber, R. J.: Fine-particle water and pH in the southeastern United States, Atmos. Chem. Phys., 15, 5211–5228, https://doi.org/10.5194/acp-15-5211-2015, 2015.

Guo, H., Sullivan, A. P., Campuzano-Jost, P., Schroder, J. C., Lopez-Hilfiker, F. D., Dibb, J. E., Jimenez, J. L., Thornton, J. A., Brown, S. S., Nenes, A., and Weber, R. J.: Fine particle pH and the partitioning of nitric acid during winter in the northeastern United States, J. Geophys. Res.: Atmos., 121, https://doi.org/10.1002/2016jd025311, 2016.

Guo, H., Weber, R. J., and Nenes, A.: High levels of ammonia do not raise fine particle pH sufficiently to yield nitrogen oxide-dominated sulfate production, Sci. Rep., 7, 12109, https://doi.org/10.1038/s41598-017-11704-0, 2017.

Hao, Q., Jiang, N., Zhang, R., Yang, L., and Li, S.: Characteristics, sources, and

reactions of nitrous acid during winter at an urban site in the Central Plains Economic Region in China, Atmos. Chem. Phys. 20, 7087–7102, https://doi.org/10.5194/acp-20-7087-2020, 2020.

Hu, B., Duan, J., Hong, Y., Xu, L., Li, M., Bian, Y., Qin, M., Fang, W., Xie, P., and Chen, J.: Exploration of the atmospheric chemistry of nitrous acid in a coastal city of southeastern China: results from measurements across four seasons, Atmos. Chem. Phys., 22, 371–393, https://doi.org/10.5194/acp-22-371-2022, 2022.

Hu, Q., Zhang, L., Evans, G. J., and Yao, X.: Variability of atmospheric ammonia related to potential emission sources in downtown Toronto, Canada, Atmos. Environ. 99, 365–373, https://doi.org/10.1016/j.atmosenv.2014.10.006, 2014.

Huang, R., Yang, L., Cao, J., Wang, Q., Tie, X., Ho, K., Shen, Z., Zhang, R., Li, G., Zhu, C., Zhang, N., Dai, W., Zhou, J., Liu, S., Chen, Y., Chen, J., and O'Dowd, C. D.: Concentration and sources of atmospheric nitrous acid (HONO) at an urban site in Western China, Sci. Total. Environ. 02, 165–172. https://doi.org/10.1016/j.scitotenv.2017.02.166, 2017.

Huy, D. H., Thanh, L. T., Hien, T. T., Noro, K., and Takenaka, N.: Characteristics of ammonia gas and fine particulate ammonium from two distinct urban areas: Osaka, Japan, and Ho Chi Minh City, Vietnam, Environ Environ. Sci. Pollut. Res. Int. 24, 8147–8163, https://doi.org/10.1007/s11356-017-8496-5, 2017.

Kleffmann, J., Kurtenbach, R., Lörzer, J., Wiesen, P., Kalthoff, N., Vogel, B., and Vogel, H.: Measured and simulated vertical profiles of nitrous acid—Part I: Field measurements, Atmos. Environ., 37, 2949–2955, https://doi.org/10.1016/s1352-2310(03)00242-5, 2003.

Kramer, L. J., Crilley, L. R., Adams, T. J., Ball, S. M., Pope, F. D., and Bloss, W. J.: Nitrous acid (HONO) emissions under real-world driving conditions from vehicles in a UK road tunnel, Atmos. Chem. Phys. 20, 5231–5248, https://doi.org/10.5194/acp-20-5231-2020, 2020.

Kurtenbach, R., Becker, K.H., Gomes, J.A.G., Kleffmann, J., Lorzer, J.C., Spittler, M., 510, and Wiesen, P., Ackermann, R., Geyer, A., Platt, U.: Investigations of emissions and heterogeneous formation of HONO in a road traffic tunnel, Atmos. Environ., 35, 3385-3394, https://doi.org/10.1016/S1352-2310(01)00138-8, 2001.

Li, D., Xue, L., Wen, L., Wang, X., Chen, T., Mellouki, A., Chen, J., and Wang, W.: Characteristics and sources of nitrous acid in an urban atmosphere of northern China: Results from 1-yr continuous observations, Atmos. Environ., 182, 296–306, https://doi.org/10.1016/j.atmosenv.2018.03.033, 2018.

Li, S., Song, W., Zhan, H., Zhang, Y., Zhang, X., Li, W., Tong, S., Pei, C., Wang, Y., Chen, Y., Huang, Z., Zhang, R., Zhu, M., Fang, H., Wu, Z., Wang, J., Luo, S., Fu, X., Xiao, S., Huang, X., Zeng, J., Zhang, H., Chen, D., Gligorovski, S., Ge, M., George, C., and Wang, X.: Contribution of vehicle emission and NO_2 surface conversion to nitrous acid (HONO) in urban environments: Implications from tests in a tunnel, Environ Sci Technol, 55, 15616–15624, https://doi.org/10.1021/acs.est.1c00405, 2021.

Li, X., Brauers, T., Haseler, R., Bohn, B., Fuchs, H., Hofzumahaus, A., Holland, F., Lou, S., Lu, K.D., Rohrer, F., Hu, M., Zeng, L.M., Zhang, Y.H., Garland, R.M., Su, H., Nowak, A., Wiedensohler, A., Takegawa, N., Shao, M., and Wahner, A.: Exploring the atmospheric chemistry of nitrous acid (HONO) at a rural site in Southern China. Atmos. Chem. Phys. 12, 1497–1513, 2012.

Liu, J., Liu, Z., Ma, Z., Yang, S., Yao, D., Zhao, S., Hu, B., Tang, G., Sun, J., Cheng, M., Xu, Z., and Wang, Y.: Detailed budget analysis of HONO in Beijing, China: Implication on atmosphere oxidation capacity in polluted megacity, Atmos. Environ., 244, https://doi.org/10.1016/j.atmosenv.2020.117957, 2021a.

Liu, M., Song, Y., Zhou, T., Xu, Z., Yan, C., Zheng, M., Wu, Z., Hu, M., Wu, Y., and Zhu, T.: Fine particle pH during severe haze episodes in northern China, Geophys. Res. Lett. 44, 5213–5221, https://doi.org/10.1002/2017gl073210, 2017.

Liu, P., Zhao, X., Zhang, C., Chen, H., Wang, J., Xue, L., Chen, J., and Mu, Y.: Fine particle pH and its influencing factors during summer at Mt. Tai: Comparison between mountain and urban sites, Atmos. Environ., 261, https://doi.org/10.1016/j.atmosenv.2021.118607, 2021.

Liu, Y., Ni, S., Jiang, T., Xing, S., Zhang, Y., Bao, X., Feng, Z., Fan, X., Zhang, L., and Feng, H.: Influence of Chinese New Year overlapping COVID-19 lockdown on HONO sources in Shijiazhuang, Sci Total Environ, 745, 141025, https://doi.org/10.1016/j.scitotenv.2020.141025, 2020.

Lv, S., Wang, F., Wu, C., Chen, Y., Liu, S., Zhang, S., Li, D., Du, W., Zhang, F., Wang, H., Huang, C., Fu, Q., Duan, Y., and Wang, G.: Gas-to-aerosol phase partitioning of atmospheric water-soluble organic compounds at a rural site in China: an enhancing effect of NH_3 on SOA formation. Environ. Sci. Technol. 56, 3915–3924, https://doi.org/10.1021/acs.est.1c06855, 2022.

Lyu, X., Wang, N., Guo, H., Xue, L., Jiang, F., Zeren, Y., Cheng, H., Cai, Z., Han, L., and Zhou, Y.: Causes of a continuous summertime O_3 pollution event in Jinan, a central city in the North China Plain, Atmos. Chem. Phys., 19, 3025–3042, https://doi.org/10.5194/acp-19-3025-2019, 2019.

Meng, F., Qin, M., Tang, K., Duan, J., Fang, W., Liang, S., Ye, K., Xie, P., Sun, Y., Xie, C., Ye, C., Fu, P., Liu, J., and Liu, W.: High-resolution vertical distribution and sources of HONO and NO_2 in the nocturnal boundary layer in urban Beijing, China, Atmos. Chem. Phys., 20, 5071–5092, https://doi.org/10.5194/acp-20-5071-2020, 2020.

Mikuska, P., Motyka, K., and Vecera, Z.: Determination of nitrous acid in air using wet effluent diffusion denuder–FIA technique, Talanta; 77, 635–641, https://doi.org/10.1016/j.talanta.2008.07.008, 2008.

Nah, T., Guo, H., Sullivan, A. P., Chen, Y., Tanner, D. J., Nenes, A., Russell, A., Ng, N. L., Huey, L. G., and Weber, R. J.: Characterization of aerosol composition, aerosol

acidity, and organic acid partitioning at an agriculturally intensive rural southeastern US site, Atmos. Chem. Phys., 18, 11471–11491, https://doi.org/10.5194/acp-18-11471-2018, 2018.

Rumsey, I. C., Cowen, K. A., Walker, J. T., Kelly, T. J., Hanft, E. A., Mishoe, K., Rogers, C., Proost, R., Beachley, G. M., Lear, G., Frelink, T., and Otjes, R. P.: An assessment of the performance of the Monitor for aerosols and gases in ambient air (MARGA): a semi-continuous method for soluble compounds. Atmos. Chem. and Phys. 14, 5639–5658, https://doi.org/10.5194/acp-14-5639-2014, 2014.

Saraswati, Sharma, S. K., Saxena, M., and Mandal, T. K.: Characteristics of gaseous and particulate ammonia and their role in the formation of secondary inorganic particulate matter at Delhi, India, Atmos. Res. 218, 34–49, https://doi.org/10.1016/j.atmosres.2018.11.010, 2019.

Seinfeld, J. H., Pandis, S. N., and Noone, K. J.: Atmospheric chemistry and physics: from air pollution to climate change. Phys. Today 51, 88–90, https://doi.org/10.1063/1.882420, 1998.

Shi, G., Xu, J., Peng, X., Xiao, Z., Chen, K., Tian, Y., Guan, X., Feng, Y., Yu, H., Nenes, A., and Russell, A. G.: pH of pH of aerosols in a polluted atmosphere: source contributions to highly acidic aerosol. Environ. Sci. Technol. 51, 4289–4296, https://doi.org/10.1021/acs.est.6b05736, 2017.

Shi, G., Xu, J., Peng, X., Xiao, Z., Chen, K., Tian, Y., Guan, X., Feng, Y., Yu, H., Nenes, A., and Russell, A. G.: pH of pH of aerosols in a polluted atmosphere: source contributions to highly acidic aerosol. Environ. Sci. Technol. 51, 4289–4296, https://doi.org/10.1021/acs.est.6b05736, 2017.

Shi, G., Xu, J., Shi, X., Liu, B., Bi, X., Xiao, Z., Chen, K., Wen, J., Dong, S., Tian, Y., Feng, Y., Yu, H., Song, S., Zhao, Q., Gao, J., and Russell, A. G.: Aerosol pH dynamics during haze periods in an urban environment in China: use of detailed, hourly, speciated observations to study the role of ammonia availability and

secondary aerosol formation and urban environment. J. Geophys. Res. Atmos. 124, 9730–9742, https://doi.org/10.1029/2018jd029976, 2019.

Song, S., Gao, M., Xu, W., Shao, J., Shi, G., Wang, S., Wang, Y., Sun, Y., and McElroy, M. B.: Fine-particle pH for Beijing winter haze as inferred from different thermodynamic equilibrium models, Atmos. Chem. Phys. 18, 7423–7438, https://doi.org/10.5194/acp-18-7423-2018, 2018.

Su, H., Cheng, Y. F., Cheng, P., Zhang, Y. H., Dong, S., Zeng, L. M., Wang, X., Slanina, J., Shao, M., and Wiedensohler, A.: Observation of nighttime nitrous acid (HONO) formation at a non-urban site during PRIDE-PRD2004 in China, Atmos. Environ., 42, 6219–6232, https://doi.org/10.1016/j.atmosenv.2008.04.006, 2008.

Takeuchi M, M. Y., Tsunoda H, Tanaka H.: Atmospheric acid gases in tokushima, Japan, monitored with parallel plate wet denuder coupled ion chromatograph. Anal. Sci. 29, 165–168, https://doi.org/10.2116/analsci.29.165, 2013.

VandenBoer, T. C., Brown, S. S., Murphy, J. G., Keene, W. C., Young, C. J., Pszenny, A. A. P., Kim, S., Warneke, C., de Gouw, J. A., Maben, J. R., Wagner, N. L., Riedel, T. P., Thornton, J. A., Wolfe, D. E., Dubé, W. P., Öztürk, F., Brock, C. A., Grossberg, N., Lefer, B., Lerner, B., Middlebrook, A. M., and Roberts, J. M.: Understanding the role of the ground surface in HONO vertical structure: High resolution vertical profiles during NACHTT-11, J. Geophys. Res.: Atmos., https://doi.org/10.1002/jgrd.50721, 2013.

VandenBoer, T. C., Markovic, M. Z., Sanders, J. E., Ren, X., Pusede, S. E., Browne, E. C., Cohen, R. C., Zhang, L., Thomas, J., Brune, W. H., and Murphy, J. G.: Evidence for a nitrous acid (HONO) reservoir at the ground surface in Bakersfield, CA, during CalNex 2010. J. Geophys. Res.: Atmos. 119, 9093–9106, https://doi.org/10.1002/2013jd020971, 2014.

Veres, P., Roberts, J. M., Burling, I. R., Warneke, C., de Gouw, J., and Yokelson, R. J.: Measurements of gas-phase inorganic and organic acids from biomass fires by

483 negative-ion proton-transfer chemical-ionization mass spectrometry., J. Geophys.
484 Res.: Atmos., 115, D23302, https://doi.org/10.1029/2010jd014033, 2010.
485 Wang, G., Zhang, R., Gomez, M. E., Yang, L., Levy Zamora, M., Hu, M., Lin, Y., Peng,
486 J., Guo, S., Meng, J., Li, J., Cheng, C., Hu, T., Ren, Y., Wang, Y., Gao, J., Cao, J.,
487 An, Z., Zhou, W., Li, G., Wang, J., Tian, P., Marrero-Ortiz, W., Secrest, J., Du, Z.,
488 Zheng, J., Shang, D., Zeng, L., Shao, M., Wang, W., Huang, Y., Wang, Y., Zhu, Y.,
489 Li, Y., Hu, J., Pan, B., Cai, L., Cheng, Y., Ji, Y., Zhang, F., Rosenfeld, D., Liss, P.
490 S., Duce, R. A., Kolb, C. E., and Molina, M. J.: Persistent sulfate formation from
491 London Fog to Chinese haze. Proc. Natl. Acad. of Sci. U. S. A. 113, 13630–13635,
492 https://doi.org/10.1073/pnas.1616540113, 2016a.
493 Wang, H., Ding, J., Xu, J., Wen, J., Han, J., Wang, K., Shi, G., Feng, Y., Ivey, C. E.,
494 Wang, Y., Nenes, A., Zhao, Q., and Russell, A. G.: Aerosols in an arid environment:
495 the role of aerosol water content, particulate acidity, precursors, and relative
496 humidity on secondary inorganic aerosols. Sci. Total Environ. 646, 564–572,
497 https://doi.org/10.1016/j.scitotenv.2018.07.321, 2019.
498 Wang, M., Wang, S., Zhang, R., Yuan, M., Xu, Y., Shang, L., Song, X., Zhang, X., and
499 Zhang, Y.: Exploring the HONO source during the COVID-19 pandemic in a
500 megacity in China, J. Environ. Sci., 149, 616–627,
501 https://doi.org/10.1016/j.jes.2023.12.021, 2025.
502 Wang, R., Ye, X., Liu, Y., Li, H., Yang, X., Chen, J., Gao, W., and Yin, Z.:
503 Characteristics of atmospheric ammonia and its relationship with vehicle
504 emissions in a megacity in China, Atmos. Environ. 182, 97–104,
505 https://doi.org/10.1016/j.atmosenv.2018.03.047, 2018.
506 Wang, S., Wang, L., Li, Y., Wang, C., Wang, W., Yin, S., and Zhang, R.: Effect of
507 ammonia on fine-particle pH in agricultural regions of China: comparison between
508 urban and rural sites, Atmos. Chem. Phys. 20, 2719–2734,
509 https://doi.org/10.5194/acp-20-2719-2020, 2020.

Wang, W., Wang, S., Xu, J., Zhou, R., Shi, C., and Zhou, B.: Gas-phase ammonia and $PM_{2.5}$ ammonium in a busy traffic area of Nanjing, China, Environ. Sci. Pollut. Res. Int., 23, 1691–1702, https://doi.org/10.1007/s11356-015-5397-3, 2016b.

Wang, X., Yin, S., Zhang, R., Yuan, M., and Ying, Q.: Assessment of summertime O_3 formation and the O_3-NO_X-VOC sensitivity in Zhengzhou, China using an observation-based model. Sci. Total Environ. 813, 152449, https://doi.org/10.1016/j.scitotenv.2021.152449, 2022.

Wang, Y., Zhu, S., Ma, J., Shen, J., Wang, P., Wang, P., and Zhang, H.: Enhanced atmospheric oxidation capacity and associated ozone increases during COVID-19 lockdown in the Yangtze River Delta, Sci. Total Environ., 768, 144796, https://doi.org/10.1016/j.scitotenv.2020.144796, 2021.

Wong, K. W., Oh, H. J., Lefer, B. L., Rappenglück, B., and Stutz, J.: Vertical profiles of nitrous acid in the nocturnal urban atmosphere of Houston, TX, Atmos. Chem. Phys., 11, 3595–3609, https://doi.org/10.5194/acp-11-3595-2011, 2011.

Wu, S., Zhang, Y., Schwab, J., Li, Y., Liu, Y., and Yuan, C.: High-resolution ammonia emissions inventories in Fujian, China, 2009–2015, Atmos. Environ., 162, 100–114, https://doi.org/10.1016/j.atmosenv.2017.04.027, 2017.

Xu, W., Kuang, Y., Zhao, C., Tao, J., Zhao, G., Bian, Y., Yang, W., Yu, Y., Shen, C., Liang, L., Zhang, G., Lin, W., and Xu, X.: NH_3-promoted hydrolysis of NO_2 induces explosive growth in HONO, Atmos. Chem. Phys. 19, 10557–10570, https://doi.org/10.5194/acp-19-10557-2019, 2019.

Xu, Z., Wang, T., Wu, J., Xue, L., Chan, J., Zha, Q., Zhou, S., Louie, P. K. K., and Luk, C. W. Y.: Nitrous acid (HONO) in a polluted subtropical atmosphere: Seasonal variability, direct vehicle emissions and heterogeneous production at ground surface, Atmos. Environ., 106, 100–109, https://doi.org/10.1016/j.atmosenv.2015.01.061, 2015.

Yang, Y., Shao, M., Keßel, S., Li, Y., Lu, K., Lu, S., Williams, J., Zhang, Y., Zeng, L.,

Nölscher, A. C., Wu, Y., Wang, X., and Zheng, J.: How the OH reactivity affects the ozone production efficiency: case studies in Beijing and Heshan, China, Atmos. Chem. Phys., 17, 7127–7142, https://doi.org/10.5194/acp-17-7127-2017, 2017.

Yu, Y., Cheng, P., Li, H., Yang, W., Han, B., Song, W., Hu, W., Wang, X., Yuan, B., Shao, M., Huang, Z., Li, Z., Zheng, J., Wang, H., and Yu, X.: Budget of nitrous acid (HONO) at an urban site in the fall season of Guangzhou, China, Atmos. Chem. Phys., 22, 8951–8971, https://doi.org/10.5194/acp-22-8951-2022, 2022.

Yun, H., Wang, Z., Zha, Q., Wang, W., Xue, L., Zhang, L., Li, Q., Cui, L., Lee, S., Poon, S. C. N., and Wang, T.: Nitrous acid in a street canyon environment: Sources and contributions to local oxidation capacity, Atmos. Environ., 167, 223–234, https://doi.org/10.1016/j.atmosenv.2017.08.018, 2017.

Zellweger, M. A., P.Hofer,U.Baltensperger.: NOy speciation with a combined wet effluent diffusion denuder–aerosol collector coupled to ion chromatography, Atmos. Environ., 33, 1131–1140, https://doi.org/10.1016/s1352-2310(98)00295-7, 1999.

Zhang, S., Sarwar, G., Xing, J., Chu, B., Xue, C., Sarav, A., Ding, D., Zheng, H., Mu, Y., Duan, F., Ma, T., and He, H.: Improving the representation of HONO chemistry in CMAQ and examining its impact on haze over China, Atmos. Chem. Phys., 21, 15809–15826, https://doi.org/10.5194/acp-21-15809-2021, 2021.

Zhang, W., Tong, S., Jia, C., Wang, L., Liu, B., Tang, G., Ji, D., Hu, B., Liu, Z., Li, W., Wang, Z., Liu, Y., Wang, Y., and Ge, M.: Different HONO sources for three layers at the urban area of Beijing. Environ. Sci. Technol. 54, 12870–12880, https://doi.org/10.1021/acs.est.0c02146, 2020a.

Zhang, Y., Liu, X., Fang, Y., Liu, D., Tang, A., and Collett, J. L.: Atmospheric ammonia in Beijing during the COVID-19 outbreak: concentrations, sources, and implications. Environ. Sci. Technol. Lett. 8, 32–38, https://doi.org/10.1021/acs.estlett.0c00756, 2020b.

564 Zhao, Y., Zhang, N., Wei, Q., Han, Y., Mao, K., Cai, Y., and Li, R.: Flow injection
565 chemiluminescence method in analytical chemistry., Spectrosc. Spectra. Anal., 30,
566 2512–2517., https://doi.org/11-2200/O4WCNKI, 2010.